

# The Spectroscopically Determined Substellar Mass Function of the Orion Nebula Cluster

Catherine L. Slesnick<sup>1</sup>, Lynne A. Hillenbrand<sup>1</sup>, & John M. Carpenter<sup>1</sup>

*Dept. of Astronomy, MS105-24, California Institute of Technology, Pasadena, CA 91125*

`cls@astro.caltech.edu, lah@astro.caltech.edu, jmc@astro.caltech.edu`

## ABSTRACT

We present a spectroscopic study of candidate brown dwarf members of the Orion Nebula Cluster (ONC). We obtained new  $J$ – and/or  $K$ –band spectra of  $\sim 100$  objects within the ONC which are expected to be substellar based on their  $K$ ,  $(H - K)$  magnitudes and colors. Spectral classification in the near-infrared of young low mass objects is described, including the effects of surface gravity, veiling due to circumstellar material, and reddening. From our derived spectral types and existing near-infrared photometry we construct an HR diagram for the cluster. Masses are inferred for each object and used to derive the brown dwarf fraction and assess the mass function for the inner  $5.1 \times 5.1$  of the ONC, down to  $\sim 0.02 M_{\odot}$ . The logarithmic mass function rises to a peak at  $\sim 0.2 M_{\odot}$ , similar to previous IMF determinations derived from purely photometric methods, but falls off more sharply at the hydrogen-burning limit before leveling through the substellar regime. We compare the mass function derived here for the inner ONC to those presented in recent literature for the sparsely populated Taurus cloud members and the rich cluster IC 348. We find good agreement between the shapes and peak values of the ONC and IC 348 mass distributions, but little similarity between the ONC and Taurus results.

*Subject headings:* infrared: stars – open clusters and associations: individual (Orion Nebula Cluster) – stars: luminosity function, mass function – stars: low-mass, brown dwarfs – stars: pre-main-sequence

---

<sup>1</sup>Visiting astronomer, W. M. Keck Observatory, which is operated as a scientific partnership among the California Institute of Technology, the university of California and the National Aeronautics and Space Administration.

## 1. Introduction

The stellar mass and age distributions in young star clusters can help answer some of the fundamental questions of cluster formation theory: Do all cluster members form in a single burst or is star formation a lengthy process? Is the distribution of stellar masses formed during a single epoch within a cluster, also known as the initial mass function (IMF), universal or does it vary with either star formation environment or time? While the stellar mass function has long been studied (e.g., Salpeter 1955), we are only recently beginning to explore the very low mass end of the distribution into the substellar regime. Identification of large, unbiased samples of low mass objects, especially in star-forming regions, is crucial to our understanding of the formation and early evolution of low mass stars and brown dwarfs.

Young stellar clusters are particularly valuable for examining the shape of the low mass IMF because the lowest mass members have not yet been lost to dynamical evolution. Furthermore, contracting low-mass pre-main sequence stars and brown dwarfs are 2-3.5 orders of magnitude more luminous than their counterparts on the main sequence, and thus can be more readily detected in large numbers. The dense molecular clouds associated with star-forming regions also reduce background field star contamination.

Because the ONC is one of the nearest massive star-forming regions to the Sun and the most populous young cluster within  $\sim 2$  kpc, it has been observed at virtually all wavelengths over the past several decades. However, only recently have increased sensitivities due to near-IR detectors on larger telescopes allowed us to begin to understand and characterize the extent of the ONC’s young stellar and brown dwarf population which, at  $\lesssim 1$ -2 Myr, is just beginning to emerge from its giant molecular cloud.

Several recent studies have explored the ONC at substellar masses. Hillenbrand & Carpenter (2000) (hereafter HC00) present the results of an  $H$  and  $K$  imaging survey of the inner  $5'.1 \times 5'.1$  region of the ONC. Observed magnitudes, colors, and star counts were used to constrain the shape of the ONC mass function across the hydrogen burning limit down to  $\sim 0.03 M_{\odot}$ . They find evidence in the log-log mass function for a turnover above the hydrogen-burning limit, then a plateau into the substellar regime. A similar study by Muench et al. (2002; hereafter M02) uses  $J, H, K$  imaging of the ONC to derive an IMF which rises to a broad primary peak at the lowest stellar masses between  $0.3 M_{\odot}$  and the hydrogen burning limit before turning over and declining into the substellar regime. However, instead of a plateau through the lowest masses, M02 find evidence for a secondary peak between  $0.03$ – $0.02 M_{\odot}$ . Luhman et al. (2000) use  $H$  and  $K$  infrared imaging and limited ground-based spectroscopy to constrain the mass function and again find a peak just above the substellar regime, but then a steady decline through the lowest mass objects.

Generally speaking,  $J$ ,  $H$ ,  $K$  photometry alone is insufficient for deriving stellar/substellar masses, though may be adequate in a statistical sense for estimating mass distributions given the right assumptions. The position of a young star in a near-IR color-magnitude diagram (CMD) is dependent on mass, age, extinction, and the possible presence of a circumstellar disk. These characteristics affect the conversion of a star’s infrared magnitude and color into its stellar mass. Unless the distributions of these parameters are known a priori, knowledge of the cluster’s luminosity function alone is not sufficient to draw definitive conclusions about its mass function. In addition, cluster membership is often poorly known and statistical estimates concerning the extent and characterization of the field star population must be derived. In the case of the densely populated ONC, it has been suggested that the field star contamination is small but non-negligible toward fainter magnitudes. HC00 used a modified version of the Galactic star count model (Wainscoat et al. 1992) convolved with a local extinction map (derived from a  $\text{C}^{18}\text{O}$  molecular line map) to estimate the field star contribution, which they found to constitute  $\sim 5\%$  of the stars down to their completeness limit at  $K \sim 17.5$ .

In order to study a cluster’s IMF in more than just a statistical sense, spectroscopy is needed to confirm cluster membership of individual stars and uniquely determine location in the HR diagram (and hence mass). We have obtained near-infrared spectra of 97 stars in the ONC. This wavelength regime (1-2.5  $\mu\text{m}$ ) is of extreme interest for very cool stars and brown dwarfs not only because ultracool objects emit the bulk of their energy in the near-infrared, but also because this regime contains temperature-sensitive atomic as well as broad molecular features. In addition, there are several diagnostic lines which can be used as surface gravity indicators. From analysis of these data combined with existing photometry and pre-main sequence evolutionary theory we construct the cluster’s IMF across the substellar boundary. We then compare our results to those found from previous studies, both of the ONC and of clusters similar in age to the ONC but which have different star-forming environments.

In Section 2 we describe our data acquisition and reduction. In Section 3 we present our spectra and methods for spectral classification. This section includes a discussion of the effects of extinction and veiling due to circumstellar disks. In Section 4 we create an HR diagram for the stellar and substellar objects for which we have new spectral types. Section 5 contains our derivation of the ONC’s IMF and Section 6 our analysis and comparison to previous work.

## 2. Observations

### 2.1. Infrared Spectroscopic Sample Selection

Candidate sub-stellar objects have been selected from the HC00 photometric survey for follow-up spectroscopy to determine if their temperatures and surface gravities are consistent with those of brown dwarf objects at the age ( $\sim 1$  Myr) and distance (480 pc) of the ONC. Figure 1 is a color-magnitude diagram showing the HC00 photometry. We transformed the isochrones and mass tracks of D’Antona & Mazzitella 1997 & 1998<sup>1</sup> (hereafter DM97) into the  $K, (H - K)$  plane and selected stars for spectroscopy based on their location in the CMD below a line which corresponds to the reddening vector originating at the hydrogen burning limit ( $M = 0.08 M_{\odot}$ ). In addition to stars selected from infrared photometry, several stars were followed-up with infrared spectroscopy before the deep HC00 data became available based on optical ( $V, I$ ) magnitudes and colors (Hillenbrand 1997; hereafter H97) indicating they might be substellar.

We obtained new infrared spectra of 97 objects within the ONC; 81 selected from the HC00 work were observed using NIRSPEC (Section 2.2.1) and 16 selected from optical magnitudes and colors were observed using CRSP (Section 2.2.2). Our sample included  $\sim 50\%$  of the stars in the HC00 survey area expected to be brown dwarfs based on their  $K, (H - K)$  magnitudes and colors, down to the completeness limit of  $K \sim 17.5$ . Often it was possible to place multiple stars on the slit due to the high stellar density of the cluster, allowing us to observe several brighter stars, some with known spectral types which could be used as secondary spectral standards.

### 2.2. Infrared Data Acquisition

#### 2.2.1. NIRSPEC Data

Near-IR spectra of candidates selected from infrared photometry were taken with the NIRSPEC spectrograph on the Keck II Telescope on Mauna Kea, Hawaii. This near-infrared spectrograph has a 1024x1024 InSb array with  $27 \mu\text{m}$  pixels. We used the low-resolution mode of the camera with an entrance slit of  $42'' \times 0.72''$ , resulting in a resolving power of  $R \sim 1400$ . Stars were placed in the entrance slit using a  $K$ -band guide camera.  $J$ -band spectra were taken on 2 & 3 February, 2002 through the NIRSPEC-3 filter which spans the wavelength range of  $1.143\text{--}1.375 \mu\text{m}$ . Typical exposure times were  $\sim 300$  s.  $K$ -band data

---

<sup>1</sup>The 1998 models are a web-only correction at  $<0.2 M_{\odot}$  to their original 1997 work.

were taken on 29 November, and 1 & 2 December, 2002, through the K' filter (1.950–2.295  $\mu\text{m}$ ). This filter offers less wavelength coverage than either the K or the NIRSPEC-7 filters; however it afforded us extremely high transmission, particularly at the short wavelength end. The K' filter has  $> 90\%$  transmission from 2–2.95  $\mu\text{m}$ , whereas the NIRSPEC-7 filter gives an average of  $\sim 80\%$  transmission (sometimes as low as 70%) in this range and the K filter gives an average of 70%. Our aim when taking the *K*-band spectra was to observe as many faint objects as possible so that we would have a statistically large enough sample of known cluster members with spectral types (and therefore, masses) from which to construct an accurate IMF. We felt it would be a more effective use of limited telescope time to use the K' filter so that we could observe more and fainter objects with shorter exposure times. We are still able to make use of 2 of the 3 molecular absorption features between 2–2.5  $\mu\text{m}$  commonly utilized for classification of low mass stars (see Section 3.1.2). Typical exposure times for the *K*-band data were 300–600 s.

For each object, we took exposures in sets of 3, nodding the star along the slit between each exposure. For our fainter targets, 2–3 sets of observations were required. In most cases we were able to observe multiple objects in a single exposure by rotating the slit position angle. Telluric reference stars were observed throughout the night over a wide range in airmass. We observed O & G stars whose spectra have relatively few absorption features in the *J* & *K*-bands at our resolution and may be used as telluric templates. NeAr arc lamp spectra and internal flats used in rectifying the images (see Section 2.3) were taken at the start and end of each night.

### 2.2.2. CRSP Data

For sources selected from optical *I*, (*V*–*I*) magnitudes and colors, spectra were obtained with the Cryogenic Infrared Spectrograph (CRSP) on the Mayall 4m telescope at Kitt Peak National Observatory on the nights of 16–19 January, 1998. The instrument is a cooled grating spectrograph with a 256x256 InSb detector. Low resolution ( $R = 1000$ ) spectra were collected using a 200 l/mm grating in the Y–, J–, H–, and K–bands (3rd, 2nd, 2nd, and 1st orders respectively). The slit subtended 1.0" with the infrared seeing typically 0.9–1.2". Stars were positioned in the slit via a visible guide camera and data were collected in a standard two-beam beam–switching mode. Integration times ranged from 0.316 (minimum read-out time) to 120 seconds for individual frames. A0 and G2 telluric standard stars were observed for correction of spectral standards while the O7 star  $\theta^1\text{C}$  Ori was used for program stars. Wavelength calibration was established from exposures of a HeNeAr arc lamp while dome–flats were collected with and without incandescent illumination of a white

screen mounted inside the telescope dome.

### 2.3. Infrared Data Reduction

#### 2.3.1. *NIRSPEC Data*

We reduced the NIRSPEC data within IRAF, applying both standard tasks and custom techniques developed for reducing NIRSPEC data. All sources, including standards, were pre-processed and extracted in the same manner as outlined below.

Bad pixel masks were created by median-combining dark exposures taken at the beginning of each night. The mask was then applied to all images within a given night using the IRAF FLVMASK task which replaces bad pixels by interpolating along the spectral direction. Cosmic rays were removed using QZAP, written by Mark Dickenson. Since raw NIRSPEC data are tilted in both the spatial and dispersion directions, we used custom IRAF software written by Gregory D. Wirth (available publicly on the NIRSPEC website) to rectify the data. This software first removes shifts in the x (spatial) direction using a spatial map, created from a flat-field exposure, to align the edge of an image along a single column. Next, arc lamp spectra are used to align emission features along image rows in the wavelength direction by applying a second-order chebyshev fit.

We did not flat field the data because we found the internal flats did not uniformly illuminate the detector in the lower resolution mode. In addition, for the *J*-band data presence of ice on the dewar window caused time-variable streaks on the flat field images in the spectral direction. While non-uniform illumination of the flat field images does not cause a large problem for observations concerned only with narrow absorption/emission lines, we are interested in the strength of broad molecular absorption bands measured as relative flux levels at different parts of the spectrum. Therefore, it is essential that the data be flat in the dispersion direction. We found using the flat-field images on the standard star observations introduced error rather than correcting it. Instead, division by a telluric reference star corrected adequately for any non-uniform features in the dispersion direction of the detector. Once the effectiveness of this method was confirmed with our sequences of standard stars, we applied it to our ONC spectra (see below).

To remove background night sky and nebular emission lines, we used one of the adjacent nod position images to create a sky frame (or an average of two nod position images). Simple image subtraction does not work for this data because the background emission varies on short timescales. Instead, we used the median value along each row to create background emission frames free from stellar continuum for both the target and sky frames.

The sky emission frame was then scaled at each row to match the relative intensities of the emission lines on the target emission frame. This new sky frame was then subtracted off the original target frame. Because our objects are located in the Orion Nebula whose spectrum contains very strong emission features which can vary on extremely small spatial scales (a few arcseconds), some residual emission/absorption areas were sometimes left after sky subtraction. To correct for these, individual background regions were determined and subtracted from the source during spectral extraction (using APALL within IRAF).

Each spectrum was wavelength calibrated using sky emission lines, except the short exposures for which the next closest observation in time was used. A telluric spectrum was produced for each extraction from a weighted average of the two flux standards closest in airmass, thereby creating a standard spectrum at the airmass of the object. For most objects we used  $\theta^1$ C Ori as the standard star both because of its near-featureless spectrum, and because its location near the center of the Orion Nebula made it easy to observe at representative airmasses. The only exceptions were some of the M-type standard stars, particularly those in Upper Sco, which were observed at airmasses  $\geq 1.6$ . For these objects we used HR4498 (G0 V) as a telluric standard after interpolating over the few detectable absorption features in its spectrum. Finally, we averaged together all spectra for a given object and multiplied by a synthetic blackbody spectrum appropriate for the temperature of the telluric standard used. The spectra were normalized to have an average flux of unity (over the entire wavelength region within the filter) for analysis.

Figure 2 shows two NIRSPEC spectra representative of the typical S/N for our program objects. We have chosen to show these objects because they were observed during both observing runs (along with HC 383, HC 509 and several of the standards) as a consistency check. In addition, they have relatively low extinction ( $A_V < 5$ ) and therefore can be more easily compared to previously published spectra of objects at the same temperatures (see Section 3.4). The few residual emission lines from the background nebula have been interpolated over. In general, we find agreement to within errors between  $J$  &  $K$ -band spectral types when both data are available. A detailed description of our spectral classification methods, including a discussion of reddening estimates is given in Section 3. Typical signal-to-noise ratios of the ONC spectra were  $\sim 10\text{--}70$  pixel $^{-1}$ , with nearly all spectra classifiable.

### 2.3.2. CRSP Data

Standard image processing was accomplished using IRAF. After linearization, image trimming, and bad pixel correction, individual beam-switched pairs of spectra were subtracted in order to effect a first-order sky subtraction and to remove dark current and

bias offsets. Normalized flat-fields were constructed from median-filtered combinations of “lights-on” minus “lights-off” dome flats, and used to flat-field the data frames. Spectra were extracted using the APALL task and combined using a flux-weighted average. The dispersion solution was derived from extracted arc spectra and individually adjusted using cross-correlation techniques to bring the spectra to a common wavelength zero point. This step was necessary due to the continual shifts of the grating required in order to obtain data in all four near-infrared atmospheric windows. To remove atmospheric and instrumentation effects from the data, the combined spectra were divided by telluric standards in which Paschen and Brackett series lines were first interpolated over. In order to preserve the intrinsic spectral energy distributions of the program stars the telluric-divided spectra were multiplied by a black-body function appropriate to the adopted telluric standard. The final spectra were normalized to have an average flux of unity over the entire spectral range. For the analysis presented herein we make use of only the J-band and K-band spectra from this data set.

#### 2.4. Optical Spectroscopy

We have compared the spectral types derived from our new infrared spectra to those obtained from optical spectra, either as presented in the tables of H97 or as newly updated by us based on data obtained with Keck II / LRIS. Data were obtained with LRIS on six different occasions between January 1998 and January 2002 by us and by additional observers including N. Reid and B. Schaefer. Both single slit and multislit modes were employed. Stars for the single slit observations were selected in a manner similar to that employed for the CRSP observations described above, namely based on location in the  $I, (V - I)$  color-magnitude diagram. The multi-slit observations were focused similarly to the NIRSPEC observations described above, primarily on the brighter substellar candidates from the  $K, (H - K)$  survey of HC00. Objects for which we have classifiable LRIS spectra are shown as starred points on Figure 1.

The grating was either a 400/8500 or 600/7500 (lines per mm / blaze) depending on the run, producing  $R \sim 1400$  spectra nominally over 6000-10500 Å with shifts in spectral coverage of up to  $\pm 1000$  Å for the multislit data. Single slit observations were typically 240-600 second integrations whereas the multi-slit data were taken in stacks of 5-8 600 second integrations in order to avoid nebular saturation perpendicular to the dispersion direction and thus across the slitlets. Data were reduced, after median filtering and stacking the multislit data, using standard techniques of bias-subtraction, flat-fielding, and spectral extraction with particular attention needed due to the strong and spatially variable nebular emission. Spectra were

classified using a depth of feature analysis as described in H97 with the TiO and VO bands the most important spectral diagnostics in the M-type range of interest in this paper.

Optical spectral types are presented in Tables 1a and 1b for comparison to our infrared spectral types. Types which are not footnoted come from the new LRIS spectra whereas footnoted types are from H97.

### 3. Infrared Spectral Classification

To ensure that we could accurately classify our program spectra we took a range of spectral main-sequence standards using NIRSPEC: M0-M9 at *J*-Band and K7-L3 at *K*-Band. We also took spectra of mid to late M lower surface gravity stars in Upper Scorpius and Praesepe as well as field giants. For the *J*-band data we were able to include electronically available standard spectra of nearby field dwarfs taken by the Leggett group<sup>2</sup> because our classification indices rely on the depth of H<sub>2</sub>O and FeH absorption features, rather than the shape of the continuum (the continuum shape was later considered in comparison to our NIRSPEC standards when possible; see Section 3.1). We did not have this luxury in the *K*-band due to the flat-field issues discussed in Section 2.3.1.

As detailed below, we rely primarily on broad-band molecular features for spectral classification. We present our spectral types for objects within the inner 5.'1×5.'1 of the ONC (centered on θ<sup>1</sup>C) in Table 1a. When possible, objects have been cross-referenced to previous literature and optical spectral types are given. Table 1a also includes estimates for the surface gravity of each object based on the presence and relative strengths of atomic absorption lines. Most (but not all – see Sections 3.1 & 3.2) of the atomic lines present in main sequence stars at similar temperatures are much weaker in the ONC spectra due to the young age and consequently lower surface gravity of the star. This effect is enhanced if there is excess continuum emission from a circumstellar disk. Therefore, we do not use the properties of these lines to classify a star except to say, if the lines are present and strong, the star is likely not an ONC member. Our procedures are discussed in Sections 3.1.1 & 3.1.2 and result in FeH, H<sub>2</sub>O-1 & H<sub>2</sub>O-2 index measurements also listed in Table 1a.

---

<sup>2</sup>See [www.jach.hawaii.edu/~skl/publications.html](http://www.jach.hawaii.edu/~skl/publications.html)

### 3.1. *J*-Band Indices

Figure 3 shows two *J*-band M dwarf standard spectra at different temperatures, taken with NIRSPEC. The strongest atomic line transitions in this wavelength regime are the pairs of K I lines at  $1.169\text{ }\mu\text{m}$ ,  $1.177\text{ }\mu\text{m}$  and  $1.243\text{ }\mu\text{m}$ ,  $1.252\text{ }\mu\text{m}$ . As can be seen, the strength of these features increases with later spectral type. This trend is illustrated for a wider range of spectral types in Leggett et al. (1996) (stars with spectral types earlier than M7) and McLean et al. (2003) (dwarfs of spectral type M6 and later). However, the depth of the lines is also highly dependent on surface gravity. Figure 4 shows four stars of spectral class M7–M8: an optically-classified dwarf star (LHS 3003), a newly classified lower surface gravity star of  $\sim 600$  Myr in Praesepe (RIZ Pr 11), an optically-classified star of  $\sim 10$  Myr in Upper Sco (USCO 128), and a newly classified (see below) Orion Star of  $\sim 1$  Myr (HC210). This figure illustrates the dramatic decrease in strength of the K I lines with decreasing surface gravity (see also McGovern et al. 2004 and Gorlova et al. 2003). We find these lines to be weak or absent in most of the ONC spectra, confirming cluster membership.

The dominant molecular absorption features are iron hydride (FeH) and water ( $\text{H}_2\text{O}$ ), the strongest bands of which are found at approximately  $1.20\text{ }\mu\text{m}$  and  $1.34\text{ }\mu\text{m}$ , respectively. Following the work of McLean et al (2000) and Reid et al (2001), we have constructed an index,  $\text{H}_2\text{O-1}$ , to measure the strength of the  $1.34\text{ }\mu\text{m}$  water absorption feature using the ratio of the flux at  $1.34\text{ }\mu\text{m}$  to that at  $1.30\text{ }\mu\text{m}$ . The positions of the flux bands have been shifted slightly from those of previous authors to avoid contamination by variable emission features which arise in the surrounding nebula and may still be present after sky subtraction in some of the spectra. In addition, we constructed a new index to measure the strength of the FeH feature using the ratio of flux at  $1.20\text{ }\mu\text{m}$  to that at  $1.23\text{ }\mu\text{m}$ . Band widths are  $100\text{ }\text{\AA}$  for the  $\text{H}_2\text{O-1}$  index and  $130\text{ }\text{\AA}$  for the FeH index. The feature and continuum bands are indicated by shaded regions on Figure 3.

We found the water index to be an excellent indicator of spectral type. The upper left panel of Figure 5 shows spectral type vs. the  $\text{H}_2\text{O-1}$  index. Here, a spectral type of 0 represents an M0 star and a spectral type of 10 represents an L0 dwarf. In all panels, filled circles & triangles represent standard star spectra taken with NIRSPEC at the same time as our program objects. Open circles are the lower resolution data ( $R \sim 400$ ) taken from the Leggett group. Despite the differences in equipment and data reduction techniques, we find excellent correlation between the two sets of data. The strength of the water index decreases systematically with decreasing spectral type. We derived a functional fit to the combined standard observations which we used to classify the Orion data. Typical errors are  $\sim 1.5$  spectral subtypes. All index fits are given in Table 2.

The upper right panel of Figure 5 shows spectral type vs. the FeH index. As can be seen,

this index works well only for a limited range in spectral type (M3–L3) where the absorption feature peaks in strength. However, stars earlier than M3 and later than L3 are classifiable by measuring the  $H_2O$ -1 index. Furthermore, it is readily apparent via visual inspection of the spectra when a star has been classified by the FeH index as an M9 but is in fact an L6. Within the spectral range of interest, the strength of the FeH index decreases systematically with spectral type, similar to the  $H_2O$ -1 index. We again derived a functional fit to the combined standard observations to be used in classifying our program objects (Table 2).

In both top panels of Figure 5 the filled triangles, which represent the lower surface gravity standard stars, correspond to objects ranging in age from  $\sim$ 600 Myr (Praesepe) to  $\sim$ 10 Myr (Upper Sco & TW Hydrae). As can be seen, we find both molecular temperature (spectral type) indices to be stable to variations in surface gravity. However, great care had to be taken in applying these indices because they are sensitive to effects from reddening and IR excess (see Sections 3.4 & 3.5). Once preliminary spectral types were derived from both the  $H_2O$ -1 and FeH indices, all objects were inspected visually and compared to standards for confirmation or minor adjustment.

### 3.2. *K*-Band Indices

Figure 6 shows a sequence of *K*-band M & L dwarf standard spectra taken with NIRSPEC. We find the strong atomic line transitions (Ca I at  $1.978\ \mu m$ ,  $1.985\ \mu m$ ,  $1.986\ \mu m$ ; Al I at  $2.110\ \mu m$ ,  $2.117\ \mu m$ ; Na I at  $2.206\ \mu m$ ,  $2.208\ \mu m$ ; Ca I at  $2.261\ \mu m$ ,  $2.263\ \mu m$  &  $2.266\ \mu m$ ) all decrease in strength with temperature. The exceptions are the NaI lines which increase in strength until late M stars and then disappear quickly by early L (see also McLean et al. 2003, 2000 and Reid et al. 2001). The  $1.98\ \mu m$  Ca I triplet as well as the Na I and Al I lines decrease in strength with decreasing surface gravity but do not disappear completely at early M spectral types, even in giant stars (Kleinmann & Hall 1986). The dominant molecular features are  $H_2O$  ( $1.90\ \mu m$ ),  $H_2$  ( $2.20\ \mu m$ ) and CO ( $2.30\ \mu m$ ).

It is common practice when classifying low mass stars from *K*-band spectra to use the strength of the  $2.30\ \mu m$  CO absorption feature. Because the K' filter used in our NIRSPEC setup begins to cut out at  $\lambda \sim 2.295\ \mu m$ , we find the depth of this feature in our data to be unreliable and therefore do not use it in classification. Again, following the work of McLean et al (2000) and Reid et al (2001), we have constructed an index to measure the strength of the very broad  $1.90\ \mu m$   $H_2O$  feature (which effects the spectra from the short wavelength end of our spectral range through  $\sim 2.1\ \mu m$ ). We define our index,  $H_2O$ -2, as the ratio of the flux at  $2.04\ \mu m$  to that at  $2.15\ \mu m$  (shown as shaded regions on Figure 6). The indices have been shifted slightly from those of other authors due to ONC nebular emission

features. A plot of spectral type vs. the  $H_2O$ -2 index is shown in the lower left panel of Figure 5. The strength of this index decreases with decreasing spectral type, similar to index behavior in the  $J$ -band. We find good correlation for objects later than  $\sim M2$ . We derived an empirical fit to the standard observations which we used to classify our program stars. Typical errors are  $\sim 1.5$  spectral subtypes. Filled squares in both lower panels correspond to low surface gravity field giant stars. Wilking et al. (2004) found their  $K$ -band water index (which incorporates both the  $1.9\ \mu m$  and  $2.5\ \mu m$   $H_2O$  absorption features) to be insensitive to surface gravity in the dwarf to subgiant range. These results are consistent with those of Gorlova et al. (2003) who compared the water index for spectral type M young cluster objects and a sample of M-type field stars. However, Wilking et al (2004) do find significant scatter in the measure of this index for giant stars. They attribute this result in part to the variable nature of late-type giants. We draw a similar conclusion for the water index of giant stars from our own, admittedly extremely limited sample (three out of four of which are Mira Variables). Since we do not have a large grid of young standard stars from which to derive our own assessment of surface gravity effects on  $K$ -band  $H_2O$  absorption, we assume those of Wilking et al. (2004) and Gorlova et al. (2003) and apply the relationship found for dwarf stars to our sample of pre-main-sequence targets.

Finally, Tokunaga & Kobayashi (1999) have shown  $H_2$  absorption to be present at  $\sim 2.20\ \mu m$  in late M and early L dwarfs. They define an index,

$$K2 = \frac{< F_{2.20-2.28} > - < F_{2.10-2.18} >}{0.5(< F_{2.20-2.28} > + < F_{2.10-2.18} >)}.$$

where  $< F_{\lambda_1-\lambda_2} >$  is the average flux between  $\lambda_1$  and  $\lambda_2$ . We use a similar index,  $H_2$ , using the integrated flux between  $\lambda_1$  and  $\lambda_2$ . A plot of spectral type vs.  $H_2$  is shown in the lower right panel of Figure 5. Because the dynamic range of this index is small and the scatter significant, we do not derive an empirical fit. However, the presence of  $H_2$  absorption is readily detected in spectra of late M and early L objects through visual inspection and was used in classification. For reference, we have included measurements of  $H_2$  in Table 1.

### 3.3. CRSP Spectra

All  $J$  &  $K$ -band ONC spectra taken with CRSP were classified using the spectral features discussed above. Differences in equipment and data reduction techniques caused an offset in the continuum shape as compared to the NIRSPEC data and therefore we could not use the same band index relations. Because we had CRSP spectra for only 16 ONC objects, we relied on visual inspection for classification. Extinction estimates were made in the same manner as for the NIRSPEC data (see Section 3.4) and object spectra were

compared to artificially reddened spectra of standard stars taken with CRSP along with the target objects. Spectral types for objects inside and outside the inner  $5.^{\circ}1 \times 5.^{\circ}1$  of the ONC are given in Table 1a and 1b, respectively. All objects have optical classifications either in the literature or from new LRIS spectra and these are also listed.

### 3.4. Extinction

As mentioned in the previous sections, the indices we use to derive spectral types are sensitive to effects from extinction which differentially reddens the spectra, thus, changing the band-to-continuum ratios. Figure 7 shows an M9 main-sequence standard star (LHS 2065) which was observed during both NIRSPEC observing runs ( $J$ - &  $K$ -band). In each panel, the top spectrum is the original data. The subsequent spectra have been artificially reddened by 5, 10 and 15 magnitudes of extinction using the IRAF *deredden* package (which incorporates the empirical selective extinction function of Cardelli, Clayton & Mathis, 1989). The flux bands for the classification indices described in Section 3.1 are shown as shaded regions and the  $K$ -band  $H_2$  absorption region is marked. We expect a systematic shift in all of the indices with increased reddening.

To determine the magnitude of this effect, we artificially reddened all standard objects by 1-20 magnitudes and re-measured each band index. We then derived empirical fits of the shift of each classification index as a function of increasing extinction. Figure 8 illustrates the resulting spectral type shift plotted as a function of  $A_V$  for all three indices. Extinction causes us to systematically classify a star later than it is using the FeH and  $H_2O$ -2 indices, and earlier than it is using the  $H_2O$ -1 index. Error bars correspond to errors in the fit, which increase with increasing  $A_V$ . As can be seen, extinction must be taken into consideration when applying the indices. We find an average value of  $A_V \sim 6$  for our objects, which would result in a spectral type shift of  $\sim \pm 2$  sub-types for all indices if not accounted for.

We use color information to derive an initial extinction estimate for each of our spectral sources. It has been shown (see Hillenbrand et al. 1998, Lada et al. 2000, and Muench et al. 2001) that  $\sim 50\%$  of sources in the ONC show signs of  $(J - H), (H - K)$  infrared excess consistent with emission from a circumstellar disk. Assuming the  $(H - K)$  excess to arise from extinction alone without taking into account infrared excess results in overestimates of  $A_V$ . Meyer, Calvet, & Hillenbrand (1997) showed that the intrinsic colors of late-K and early-M stars with disks are confined to a classical T Tauri (CTTS) locus in the  $(J - H), (H - K)$  color-color plane. Following the work of M02, we derive individual reddening *estimates* for each star by dereddening its  $(J - H), (H - K)$  colors back to this CTTS locus. Stars falling below this locus (primarily due to photometric scatter) are assumed to have an  $A_V=0$ . For

12 of the objects which have no  $J$  magnitudes available,  $A_V$ 's were estimated by dereddening  $K$ ,  $(H - K)$  magnitudes and colors back to a theoretical 1 Myr isochrone.

Because the HC00 data set does not include  $J$ -band photometry, we used the color data of M02 for de-reddening purposes. In comparing the two photometric data sets, M02 & HC00, we derived  $1\sigma$  standard deviations of  $\sim 0.35$  for the  $H$  &  $K$  magnitudes. The scatter appears to be random for the  $K$  magnitudes, but M02's  $H$  photometry is systematically brighter than HC00's. Scatter between the two data sets was also noted by M02 who attributed the difference, in part, to the intrinsic infrared variability of low mass PMS stars. Variables in the Orion A molecular cloud have been found to have an average amplitude change of  $\sim 0.2$  mag at near-IR wavelengths on weekly to monthly scales (Carpenter, Hillenbrand & Strutskie 2001). M02 also noted that because of the strong nebular background, differences in aperture sizes will contribute to photometric noise.

For each program object we apply the empirical fits shown in Figure 8 to de-redden the measured spectral typing indices, and then use the new value to derive an estimate of spectral type. We compare each spectrum to standard stars, artificially reddened to the same extinction value. All spectral types were verified visually to avoid contamination of band index measurements arising from noise in the spectra.

A possible bias in the above analysis is that the CTTS locus of Meyer, Calvet & Hillenbrand (1997) applies to the Taurus cluster, where most of the stars have spectral types K7-M0. When applying the locus to stars outside this spectral range, we must take into account its anticipated width. Figure 9 is a  $(J - H), (H - K)$  color-color diagram for all of our ONC stars with spectral types (excepting 12 stars for which there was no  $J$ -band data available). The top dashed line is the CTTS locus for Taurus stars, which defines an upper bound to the locus when we consider all stars with spectral types K7-L3. The bottom dashed line defines a lower bound to this locus. The width of the region corresponds to a  $\Delta A_V$  of  $\sim 2$ , or  $\sim 0.5$  spectral subtype uncertainty (see Figure 8). Since intrinsic spectral type errors derived from the indices are  $\approx 1.5$ – $2$  subtypes, ignoring this effect does not result in significant biases. In referring to the width of the locus we have only considered how the CTTS line as defined by Meyer, Calvet & Hillenbrand (1997) would shift if it applied to stars with K7-L3 spectral types; we have not accounted for the intrinsic width of the locus as it is defined, nor for any possible shift in slope of the locus with spectral type. We emphasize that we are using this method to derive an  $A_V$  *estimate* only, to aid us in spectral classification. For placement of a star on the HR diagram more precise extinction values are derived by combining a star's photometric and spectroscopic data (see Section 4.1).

### 3.5. Infrared Excess

As mentioned previously, we expect  $\sim 50\%$  of the ONC sources to have a wavelength-dependent infrared excess due to thermal emission from warm dust grains in a circumstellar disk. This excess dilutes (veils) the strength of molecular absorption features used in spectral classification. From experiments with artificially veiled standard stars, we find that veiling can make a later-type spectrum look like an earlier-type photosphere. However, since the photospheric flux of late-type stars peaks at  $1\text{--}1.5\ \mu\text{m}$ , we do not expect extremely large excesses at near-IR wavelengths. The veiling index is defined as  $r_\lambda = F_{\lambda excess}/F_{\lambda photosphere}$ . Meyer, Calvet & Hillenbrand (1997) found that K7-M0 classical T Tauri stars have a median veiling value of  $r_K \approx 0.6$ . We expect this value to be lower for cooler objects whose photospheric emission peaks at longer near-infrared wavelengths.

Fig 10 shows the expected color excess for stars of varying spectral type veiled by a  $T=1500\ \text{K}$  blackbody. Data points are labeled by spectral type and the two rows correspond to  $r_K = 0.5$  (bottom) & 1 (top). As can be seen, for  $r_K < 0.5$ , we expect color excesses  $\Delta(H-K) \& \Delta(J-H) \lesssim 0.2\ \text{mag}$ . The effect on classification is  $\approx 1.5\text{--}2$  spectral subclasses earlier/later for the H<sub>2</sub>O-2 & FeH/H<sub>2</sub>O-1 indices. This result is somewhat over-estimated for later spectral types (cooler than  $\sim M6$ ) with  $K$ -band spectra for which it is more readily apparent via visual inspection when veiling is affecting spectral classification. Because we have no way to independently measure veiling in our spectra (modeling of high dispersion data is required), we simply note the possible bias.

### 3.6. Summary of Spectral Classification

In all cases, classification was done first using flux ratios of broad molecular absorption lines to continuum, then comparing visually to standards. Extinction was estimated assuming CTTS colors and taken into account during the classification process. The influence of veiling was investigated but not explicitly accounted for during spectral classification. Surface gravity was assessed visually from the presence/strength of atomic absorption lines. For  $J$ -band spectra an object was given a gravity classification of “low” if it had no detectable atomic absorption lines and “high” if it had strong lines, similar to those seen in spectra of dwarf standards of the same spectral type. A classification of “int” indicates absorption lines were present but not as strong as those in dwarf stars at the same temperatures (see Table 1a). For  $K$ -band spectra gravity determinations were given based on the relative strength of atomic absorption features.

From the NIRSPEC data, we have classified 71 objects in the inner ONC found to be of

spectral type K7 or later,  $\approx$ 50% of which are M6 or later. At an age of 1-2 Myr, all objects with spectral types later than M6 are substellar ( $M < 0.08 M_{\odot}$ ) based on comparison with theoretical models (e.g., DM97). In addition, we have classified 16 spectra of objects in the inner and outer parts of the nebula taken with CRSP, 9 of which are M6 or later. Finally, we also report in Tables 1a & 1b new optical spectral types obtained with LRIS, as well as those reported previously in the literature. For the large majority of sources there is excellent agreement (to  $< 2$  spectral subclasses) between optical and infrared spectral types.

#### 4. HR Diagram

In this section we combine each object’s spectral type and near-IR photometry to derive values for its luminosity and effective temperature and place it on the theoretical HR diagram. The goal is to transform temperatures and luminosities into ages and masses using theoretical pre-main sequence evolutionary tracks. From this information we can explore the ONC’s IMF down to  $< 0.02 M_{\odot}$  using spectroscopically-confirmed cluster members.

##### 4.1. Effective Temperatures, Intrinsic Colors & Bolometric Luminosities

Spectral types of K7-L3 were converted to temperatures based on the scales of Wilking, Green & Meyer (1999), Reid et al. (1999) and Bessell (1991). An empirical fit for  $BC_K$  was determined from the observational data of Leggett et al. (1996, 2002) (spectral types M1-M6.5, M6-L3). We determined intrinsic colors by computing empirical fits to a combination of Bessell & Brett (1988) theoretical models (for spectral types K7-M6) and Dahn et al. (2002) observed data (spectral types M3.5-L3).  $(H - K)$  color-excesses were converted to  $A_K$  using the reddening law of Cohen et al. (1981). Because  $J$  magnitudes are not available for all program stars, for consistency we used  $(H - K)$  colors and  $K$  magnitudes from HC00 to determine extinction values and estimate bolometric corrections. Using  $(H - K)$  colors rather than  $(J - H)$  colors to predict extinction results in higher derived  $A_V$  estimates by an average of  $\sim 3$  mag for our data ( $\sim 0.2$  mag in  $A_K$ ). In addition, if the object has substantial infrared excess, its  $K$ -band magnitude will be brighter than the photosphere. However, the combination of these effects does not produce a significant shift in placement of a star on the HR diagram. We find an average difference of  $\Delta \log L \approx 0.05$  between luminosities derived using  $J, (J - H)$  vs.  $K, (H - K)$  for objects with both  $J$ - and  $K$ -band data available. A similar trend of comparable magnitude results if we compare  $A_V$  values derived from  $(H - K)$  colors alone rather than using both  $(J - H)$  and  $(H - K)$  to deredden stars back to the CTTS locus (see Section 3.4). The uncertainty in derived  $A_V$  for an M6 star with large color

and spectral type uncertainties ( $\sigma_{(H-K)} \sim 0.05$  mag and  $\sigma_{SpecType} \sim 2$  subclasses) is  $\approx 1.5$  magnitudes. All fits are given in Table 2 and derived quantities for stars included in the HR diagram are given in Table 3.

For all derived quantities discussed above, we used dwarf scales despite the lower surface gravity of young pre-main-sequence stars. It has been known since the earliest work on T Tauri stars (Joy 1949) that young, pre-main-sequence objects are observationally much closer to dwarfs than to giants or even sub-giants. Since to date there is no accurate temperature or bolometric correction scale for pre-main-sequence stars, we use the higher gravity dwarf scales in our analysis.

#### 4.2. HR Diagram for objects with NIRSPEC data

In Figure 11 we present an HR diagram for those objects within the inner  $5.^{\circ}1 \times 5.^{\circ}1$  of the ONC (survey area of HC00) for which we have new spectral types. Objects which were classified using spectra from different instruments are plotted as different symbols. Surface gravity assessment is indicated and a typical error bar for an  $M6 \pm 1.5$  star is shown in the lower left corner. The pre-main-sequence model tracks and isochrones of DM97 are also shown. Figure 11 illustrates that we are able to probe lower masses than previous spectroscopic studies have, down to  $0.02 M_{\odot}$ .

From examination of Figure 11, it appears that we are exploring two separate populations: the inner ONC at  $\lesssim 1$  Myr, and an older population at  $\sim 10$  Myr. None of the members of this apparently older population have gravity features which indicate they might be foreground M stars. Spectra of these objects indicate instead that they have low surface gravity consistent with young objects, and are therefore also candidate cluster members. For the remainder of Section 4.2 we will discuss the possible explanations for this surprising population. First, we detail possible systematics in the data reduction/analysis which could, in principle, cause one to “create” older stars in the HR diagram. Next we discuss their possible origin if they are a real feature and finally we determine why they may not have been detected in previous studies.

There are two possible reasons we might erroneously detect a bifurcation of the HR diagram: either the spectral types are in error and the objects are actually cooler than they are shown to be here, or their luminosities have been underestimated. The photometric uncertainties for these objects are  $< 0.2$  mag for both  $H, K$  in the HC00 data and  $< 0.4$  mag for  $J, H, K$  in the M02 data. The two data sets agree to within 0.8 mag for all objects and variability, if present, is expected to be  $\sim 0.2$  mag (see Section 3.4). An object with

spectral type M2 would need to be  $\sim 3$  magnitudes brighter in  $K$ , or have its extinction underestimated by  $> 30$  mag in order to move on the HR diagram from the 10 Myr isochrone to the 1 Myr isochrone. Even taking into account the above uncertainties and possible variability, errors of this order are not possible. Moreover, if the photometry were in error, we would expect the result to be continuous scatter in the HR diagram, rather than two distinguishable branches.

The other way to account for the apparently older population through error is if the temperature estimates are too hot, i.e., the spectral types too early, in some cases by as much as 7 spectral subclasses. All spectra have been checked visually by multiple authors (C.L.S & L.A.H.) to ensure accurate classification and we believe our spectral types are robust to within the errors given. None of the possible biases resulting from assumptions made regarding veiling, extinction or gravity can have a large enough effect to produce a spectral type offset of this magnitude. One possible exception is that a mid-M (M5) K-band spectrum with high reddening can have the same appearance and band index measurements as a later-M (M7) spectra with intermediate reddening. But this phenomenon could only affect a small subset of the lower branch population. Therefore, while it may reduce slightly the number of apparent older objects, it cannot correct for them entirely.

The accuracy of our spectral types is supported by the excellent agreement of our near-IR spectral classifications with existing optical spectral types (most agree to within 2 spectral subclasses; see Table 1a). We find a significant fraction of the spectra taken with LRIS (filled triangles on Figure 11) which were classified in a completely independent manner from the NIRSPEC and CRSP data also resulted in several apparently 10 Myr old stars. If the older population arises from systematics in the reduction or spectral classification of our infrared spectra, we would not expect to find stars classified optically to fall on the same place in the HR diagram.

If we are to accept the bifurcation as a real feature in the HR diagram, several scenarios could, in principle, account for it. The first is that we are seeing contamination from foreground field stars. However, as mentioned, HC00 found the expected field star contribution to be only  $\sim 5\%$  down to the completeness limit of  $K \sim 17.5$  (see Section 1). We find the apparent low luminosity population to account for a much larger fraction ( $\approx \frac{1}{3}$ ) of our sample. The second possibility is that we are seeing contamination by a foreground population of M stars not from the field, but from the surrounding OB association. The ONC (also known as Orion subgroup Id) is neighbored by three somewhat older subgroups of stars (Ia, Ib, & Ic; see Brown, de Geus & de Zeeuw 1994 for a detailed description of each) which are located at distances ranging from  $\sim 360$ –400 pc and having ages (derived from high mass populations) from  $\sim 2$ –11.5 Myr. The most likely subgroup from which we would see contamination in our

data is subgroup Ic, which is located along the same line of sight as the ONC. However, its members are thought to be only  $\sim 2$  Myr old and therefore cannot account for the stars on the lower branch in the HR diagram unless their age estimate is in error. The only known part of the OB association which could be contributing  $\sim 10$  Myr old stars to our study is subgroup Ia, which is estimated to be  $\sim 11.4$  Myr.

While the known high mass population of the Ia subgroup does not extend spatially as far as the ONC, if there has been dynamical relaxation, it is possible that its lower mass members may occupy a more widespread area than the OB stars. Brown, de Geus & de Zeeuw (1994) found the initial mass function for the subgroups to be a single power law of the form  $\xi(\log M) \propto M^{-1.7 \pm 0.2}$  based on the high mass population ( $M > 4 M_{\odot}$ ). Since the lower mass members have not yet been identified or studied in detail, we extrapolate the high-mass IMF to determine the total number of stars in subgroup Ia expected down to  $0.02 M_{\odot}$  and find there should be  $\approx 3500$  members. This number is an upper limit since we have not applied a Miller-Scalo turnover to the IMF but simply extended the power law form. The angular size of the Orion Ia subgroup as studied by Brown, de Geus & de Zeeuw (1994) corresponds to a linear size of  $\sim 45$  pc. From this we can calculate a relaxation time for the cluster

$$t_{\text{relax}} = n_{\text{relax}} \times t_{\text{cross}} = \frac{8 \ln N}{N} \times \frac{R}{\sigma}.$$

Assuming a gravitationally bound cluster and a velocity dispersion of  $\sigma \sim 2$  km s $^{-1}$  consistent with the ONC (Jones & Walker 1988), we find a crossing time for the Orion Ia cluster of  $\sim 11$  Myr and a relaxation time of  $\sim 600$  Myr. Clearly the cluster is not yet dynamically relaxed and it is unlikely that its low mass population would have spread significantly past its higher mass members. This calculation does not however, rule out the possibility that the lower mass population formed over a wider spatial area than the massive stars, given that primordial mass segregation has been observed in other young clusters.

From the same IMF extrapolation we find the surface density of  $0.5\text{--}0.02 M_{\odot}$  objects in subgroup Ia to be  $\sim 2.5$  pc $^{-2}$ . The areal extent corresponding to the angular size of our survey region (assuming a distance of 480 pc) is  $\sim 0.5$  pc $^2$ . Assuming a constant surface density across this area we would expect to find  $< 2$  members of Orion Ia in the current work. Even if we ignore previous age estimates, assume all three of the subgroups could be contributing to the observed lower branch of the HR diagram, and repeat the above calculation for subgroups Ib & Ic, we would expect to see  $< 10$  stars total. Therefore, it is unlikely that the lower branch we see in the inner ONC HR diagram is purely due to contamination from surrounding populations. We cannot rule out that there may exist a foreground population of  $\sim 10$  Myr stars which is not associated with the ONC, but which was missed by the Brown, de Geus & de Zeeuw (1994) work due to its dearth of OB stars.

However, the probability that this population would lie in exactly the same line of sight as the ONC is small.

Another possible cause of the older branch of the HR diagram is scattered light from circumstellar disks and envelopes. Most of the objects in the lower branch of the HR diagram have  $(J - H), (H - K)$  near-infrared excesses consistent with their being young objects surrounded by circumstellar material which could result in their detection primarily in scattered light. If true, extinctions, and consequently luminosities for these objects would be underestimated, making them appear older than the bulk of the population. Similar arguments have been put forth by Luhman et al. (2003b) to explain low-lying stars on the HR diagram of IC 348. One uncertainty in this argument is that if scattered light is responsible for causing the apparently older population, it would have to be acting on our observations in such a way so as to create a dichotomy of object luminosities rather than a continuous distribution of stars at unusually faint magnitudes. This scenario could occur however, if the lower luminosities measured for this population are caused by a drop in observed light due to the objects being occulted by a disk. The relatively low luminosities of substellar objects would make such systems more difficult to detect and we may be observing the brighter end of a distribution of low mass scattered light sources. In support of this argument, one of these sources is coincident with an optically identified *Hubble Space Telescope* “proplyd” (which is known to be a photoevaporating circumstellar disk), and two with disks seen optically in silhouette only (Bally, O’Dell, & McCaughrean 2000).

If the lower luminosity population in the inner ONC is real, rather than due to systematics in the data reduction/analysis or contamination from the surrounding older association, the question arises as to why it was not seen in previous surveys. The deepest optical photometric survey in this inner region is that by Prosser et al. (1994) which is reported complete to  $V \approx 20$  mag and  $I \approx 19$  mag, though no details are given on how these numbers were derived or how they might vary with position in the nebula. One can view the photometric data of H97, which is a combination of ground-based CCD photometry out to 15' from the cluster center and the Prosser et al. (1994) HST CCD photometry in the inner 3' or so, in terms of color-magnitude diagrams binned by radial distance from the cluster center. At all radial distances there are some stars which sit low in the color-magnitude diagram. However, it is only in radial bins beyond  $\sim 7'$  that a substantial population (though still disproportionately small compared to our current findings) of apparently 10 Myr old low mass ( $0.1-0.3 M_{\odot}$ ) stars begins to appear, as might be expected if they are contaminants from the Orion Ic association. The inner radial bins do not display this population, though it should have been detected at masses larger than  $0.15 M_{\odot}$  *in the absence of extinction*. Notably the apparently 10 Myr old population in Figure 11 does not lack extinction. Figure 12 shows a histogram of extinction for sources included in Figure 11. The open histogram indicates all

objects; the hatched and shaded histograms include only the 1 and 10 Myr old populations, respectively. We find all three populations to have similar, roughly constant distributions for  $A_K \lesssim 0.6$  ( $A_V \lesssim 10$ ) giving further evidence that the lower luminosity branch of the HR diagram is likely not a foreground population. Accounting for typical errors ( $\sim 0.1$  mag at  $K$  and  $\sim 1.5$  mag at  $V$ ; see Section 4.1) will not change our conclusions. For extinction values larger than about 2 visual magnitudes the 0.15–0.5  $M_\odot$  stars at 10 Myr in Figure 11 would have been missed by the optical Prosser et al. (1994) photometric survey but uncovered in later infrared surveys. Further, Walker et al. (2004) find from theoretical work a lower incidence of disk occultation for higher mass CTTS ( $\sim 20\%$  of systems with disks) in comparison to lower mass substellar objects (up to  $\sim 55\%$  of systems with disks) due to smaller disk scale heights and less disk flaring. Therefore, if the low luminosity objects are a population of scattered light sources we might expect to observe smaller numbers of them at higher masses.

## 5. The Low-Mass IMF

In this section we use theoretical mass tracks and isochrones to determine a mass and age for each object in our HR diagram. In Section 5.1 we discuss our choice of models and in Section 5.2 the different criteria we consider for including a star in the IMF. Finally, in Section 5.3 we present the derived mass function and point out important features.

### 5.1. Models and Mass Estimates

Currently, there are relatively few sets of pre-main-sequence (PMS) evolutionary models which extend into the substellar regime. The Lyon group (see Baraffe et al. 1998 & Chabrier et al. 2000) calculations cover 0.001–1.2  $M_\odot$ , but do not extend to the large radii of stars younger than 1 Myr. Thus, they must be applied to young low-mass star forming regions with caution. The other widely utilized set of low-mass PMS models are those by DM97. These models cover 0.017–3.0  $M_\odot$  over an age range of  $7 \times 10^4$  yr to 100 Myr, and are therefore representative of even extremely young regions. A detailed analysis and comparison of the models is given by Hillenbrand & White (2004). For the purpose of the current work we use DM97 tracks and isochrones to determine masses and ages for stellar and substellar objects in our HR diagram.

## 5.2. Completeness

Because the ONC is highly crowded and extremely nebulous, we must be certain that the spectroscopic sample is representative of the population as a whole. Figure 13 shows a histogram of completeness as a function of magnitude. Open and hatched histograms indicate the distribution of HC00 photometry and of sources for which we have spectral types, respectively. The hatched histogram includes not only sources for which we have new spectral types, but also optically-classified sources from the literature (H97 and references therein) which fall within our survey region and were determined to be of spectral type M0 or later. In combining the two data sets our goal is to assemble a statistically large sample of cool, spectroscopically confirmed ONC members down to extremely low masses ( $M \sim 0.02 M_{\odot}$ ) from which to create our IMF.

The dotted line indicates fractional completeness with  $\sqrt{N}$  errorbars. We estimate that we are  $\sim 40\%$  complete across our magnitude range with the exception of the  $12.5 < K < 15$  bins. Undersampling at these intermediate magnitudes is caused by our combining the sample of brighter, optically-classified, mainly stellar objects with our sample of infrared-classified objects where the aim was to observe objects fainter than the substellar limit. Therefore, magnitude bins corresponding to masses near the hydrogen burning limit are underrepresented. We can correct for this by determining the masses which correspond to objects in the depleted magnitude bins. We then add stars to those mass bins according to the fractional completeness of the magnitude bins they came from, relative to the overall 40% completeness. We discuss both the corrected and non-corrected IMFs in the next section.

## 5.3. The Stellar and Substellar IMF

Figure 14 shows the mass function for stars within the inner  $5.^{\circ}1 \times 5.^{\circ}1$  of the ONC that have spectral types derived from either infrared or optical spectral data later than M0. The thick-lined open histogram, shown with  $\sqrt{N}$  errorbars, includes all stars meeting this criteria which were not determined to have high surface gravity (see Table 1a). In total, the IMF sample includes  $\sim 200$  stars and contains objects with masses as high as  $\sim 0.6 M_{\odot}$  and as low as  $< 0.02 M_{\odot}$ . Mass completeness (to the 40% level) extends from  $\sim 0.4 M_{\odot}$  (corresponding to an M0 star at 1 Myr; see Figure 11) to the completeness limit of HC00,  $\sim 0.03 M_{\odot}$  for  $A_V < 10$ . The dotted open histogram indicates an IMF for the same sample, where we have corrected for the incomplete magnitude bins. The most substantial correction occurs right at the substellar limit as indicated in Section 5.2. The hatched histogram represents only those objects determined to be younger than 5 Myr from HR diagram analysis. Thus we remove any possible bias occurring by inclusion of the apparently

older  $\sim 10$  Myr population which may or may not be a real part of the cluster. As can be seen, the apparently older stars constitute a relatively uniformly spaced population across the mass range we are exploring (see also Figure 11), and including them in the IMF does not affect our interpretation.

The stellar-substellar IMF for the inner ONC in Figure 14 peaks at  $\sim 0.2 M_{\odot}$  and falls across the hydrogen-burning limit into the brown dwarf regime. Using the observed IMF we find  $\sim 17\%$  (39) of the objects in our sample to be substellar ( $M < 0.08 M_{\odot}$ ). Below  $\sim 0.08 M_{\odot}$  the mass distribution levels off through our completeness limit of  $\sim 0.02 M_{\odot}$ . There may be a secondary peak at  $\sim 0.05 M_{\odot}$ . Decreasing the bin size by 50% yields the same results, with the peak at  $0.05 M_{\odot}$  becoming even more pronounced. Increasing the binsize by 50% produces a steady decline into the substellar regime. The total mass inferred between  $0.6 - 0.02 M_{\odot}$  from our data is  $\sim 41 M_{\odot}$  which, corrected for our 40% completeness factor becomes  $\approx 100 M_{\odot}$ . This value is a lower limit because we have already shown that we are not 40% complete at all magnitudes. We find an average mass of  $\sim 0.18 M_{\odot}$  corresponding to the peak in our data.

## 6. Discussion

### 6.1. Comparison to previous ONC IMF determinations

The stellar/substellar IMF has been discussed in previous work on the ONC. A determination based on near-infrared photometric data was made by HC00 using  $H$  and  $K$  magnitudes and colors combined with star count data to constrain the IMF down to  $\sim 0.03 M_{\odot}$ . They find a mass function for the inner regions of the ONC which rises to a peak around  $0.15 M_{\odot}$  and then declines across the hydrogen burning limit with slope  $N(\log M) \propto M^{0.57}$ . M02 transform the inner ONC's  $K$ -band luminosity function into an IMF and find a mass function which rises with decreasing mass to form a broad peak between  $0.3 M_{\odot}$  and the hydrogen-burning limit before turning over and falling off into the substellar regime. This decline is broken between  $0.02$  and  $0.03 M_{\odot}$  where the IMF may contain a secondary peak near the deuterium burning limit of  $\sim 13 M_{Jup}$ . Luhman et. al (2000) combined near-infrared NICMOS photometry of the inner  $140'' \times 140''$  of the ONC with limited ground-based spectroscopy of the brightest objects ( $K < 12$ ) to determine a mass function which follows a power-law slope similar, but slightly steeper than the Salpeter value, until it turns over at  $\sim 0.2 M_{\odot}$  and declines steadily through the brown dwarf regime. H97 presents the most extensive spectroscopic survey of the ONC, combining optical spectral data with  $V$  and  $I$ -band photometry over a large area ( $\sim 2.5 \text{ pc}^2$ ) extending into the outer regions of the cluster. The IMF determination covers a large spectral range and appears to be rising from the high (50

$M_{\odot}$ ) to low ( $0.1 M_{\odot}$ ) mass limits of that survey.

The peak in our IMF,  $\sim 0.2 M_{\odot}$ , matches remarkably well to those found from both the deep near-infrared imaging IMF studies (HC00 and M02) which cover similar survey areas, and the Luhman et al. (2000) study which covered only the very inner region of the cluster. Our data also show a leveling off in the mass distribution through the substellar regime similar to that found by HC00. A significant secondary peak within the substellar regime has been claimed by M02. While we see some evidence for such a peak in our data, this result is not robust to within the errors. Furthermore, if real, we find the secondary peak to occur at a slightly higher mass than M02 ( $\sim 0.05 M_{\odot}$  vs.  $\sim 0.025 M_{\odot}$ ). The primary difference between the observed IMF derived in the current work and those presented in previous studies of the substellar ONC population is the steepness of the primary peak and the sharpness of the fall-off at the hydrogen-burning limit (see for comparison Figure 16 of M02). Most IMF determinations for this region exhibit a gradual turnover in the mass function around  $\sim 0.2 M_{\odot}$  until  $\approx \frac{2}{3}$  the level of the primary peak is reached at which point the IMF levels off or forms a secondary peak. However, we find a sharp fall-off beyond  $\sim 0.1 M_{\odot}$  to  $\approx \frac{1}{2}$  the primary peak value.

## 6.2. Photometric vs. Spectroscopic Mass Functions

As mentioned in Section 1, spectroscopy is needed to study a cluster’s IMF in more than a statistical sense. The fact that many of the fainter objects in our survey expected to be substellar based on their location in the  $K$ ,  $(H - K)$  diagram are in fact hotter, possibly older objects gives strong evidence in support of this statement. Independent knowledge of an individual star’s age, extinction and infrared excess arising from the possible presence of a circumstellar disk is needed before definitive conclusions can be drawn about that object’s mass. Despite the increasing numbers of brown dwarfs studied, both in the field and in clusters, details of their formation process remain sufficiently poorly understood that knowledge of near-infrared magnitudes and colors alone is not enough to accurately predict these characteristics for young low mass objects. Near-infrared magnitudes alone also cannot distinguish between cluster members and nonmembers, and field star contamination must be modeled rather than accounted for directly.

Previous studies of the ONC had spectroscopy available in general only for the stellar population, and relied on photometry alone to determine the mass function at substellar masses. This may have caused over-estimates in the number of brown dwarfs for reasons discussed above. However, the more significant cause of the shallower peak in previous IMF determinations for the inner ONC as opposed to the sharply peak IMF derived here is

likely just the inherent nature of photometric vs. spectroscopic mass functions. Determining masses for stars in a sample from temperatures derived from spectral types necessarily discretizes the data. Conversely, photometric studies are by their nature continuous distributions, and deriving masses from magnitudes and colors or luminosity functions results in a smooth distribution of masses. We emphasize that while neither situation is ideal, mass functions derived for young objects from infrared photometry alone represents only the most statistically probable distribution of underlying masses. Spectroscopy is needed in order to derive cluster membership and masses for individual objects.

### 6.3. Comparison to Other Star-Forming Regions

Diagnostic studies of stellar populations in different locations and at varying stages of evolution are needed to explore the possibility of a universal mass function. While one might expect that the IMF should vary with star formation environment, we do not yet have enough evidence to determine if such a variation exists. Aside from work already mentioned on the ONC, numerous studies have been carried out to characterize the low mass stellar and substellar mass functions of other young clusters in various environments. Because of the intrinsic faintness of these objects, most surveys are photometric. Authors then use a combination of theoretical models and statistical analysis to transform a cluster's color-magnitude diagram or luminosity function into an IMF which may or may not accurately represent the underlying cluster population (see Section 6.2).

However, the substellar populations of two other young star-forming clusters have been studied spectroscopically using techniques similar to those presented here. Luhman (2000), Briceño et al. (2002) and Luhman et al. (2003a) surveyed the sparsely-populated Taurus star-forming region, and Luhman et al. (2003b) studied the rich cluster IC 348. These clusters have ages similar to the ONC (1 and 2 Myr). Therefore, if the IMF is universal, similar mass distributions should be observed for all three clusters. Contrary to this hypothesis, Luhman et al. (2003b) discuss the very different shapes of the substellar mass distributions in Taurus and IC 348. The IMF for Taurus peaks around  $\sim 0.8 M_{\odot}$  and then declines steadily to lower masses through the brown dwarf regime. The IC 348 mass function rises to a peak around  $0.15 M_{\odot}$  and then falls off sharply and levels out for substellar objects. While direct comparison of the data requires caution given that different mass tracks were used for the two studies (Luhman et al. (2003b) used Baraffe et al. (1998) tracks whereas we have used DM97 tracks to infer masses), we find our that IMF for the ONC bears remarkable resemblance to that presented for IC 348 in Luhman et al. (2003b) (see for comparison Figure 12 in Luhman et al. 2003b). Both IMFs peak at  $\sim 0.15\text{--}0.2 M_{\odot}$  and fall off rather abruptly at

the substellar boundary. The fact the IMFs derived for these two dense, young clusters bear such close resemblance to each other while exhibiting distinguishable differences from the IMF determined for the much more sparsely- populated Taurus cluster gives strong support to the argument put forth by authors such as Luhman et al. (2003b) that the IMF is not universal, but may instead depend on star formation environment. Alternatively, Kroupa et al. (2003) argue through numerical simulation that observed differences in the Taurus and ONC *stellar* mass functions could be due to dynamical effects operating on initially identical IMFs; however, their model does not reproduce the observed differences in *substellar* mass functions without invoking different initial conditions (eg., turbulence; Delgado-Donate et al. 2004).

Previous studies such as those mentioned above have found much higher brown dwarf fractions for the ONC in comparison to other clusters such as Taurus and IC 348 (see Luhman et al. 2003b). Briceño et al. (2002) defines the ratio of the numbers of substellar and stellar objects as:

$$R_{SS} = \frac{N(0.02 \leq M/M_{\odot} \leq 0.08)}{N(0.08 < M/M_{\odot} \leq 10)}.$$

We have recomputed these numbers for Taurus and IC 348 using the DM97 models and find values of  $R_{SS} = 0.11$  (Taurus) and  $R_{SS} = 0.13$  (IC 348). These values are very close to those found by Luhman et al. (2003b) using the Baraffe et al. (1998) models:  $R_{SS} = 0.14$  (Taurus) and  $R_{SS} = 0.12$  (IC 348). In contrast, Luhman et al. (2000) find a value of  $R_{SS} = 0.26$  from primarily photometric work on the inner ONC (using Baraffe et al. (1998) models). Considering the spectroscopic IMF presented here (Figure 14), we find a lower value of  $R_{SS}=0.20$ , indicating that although the ONC may have a higher brown dwarf fraction than Taurus or IC348, it is lower than previously inferred from photometric studies.

## 7. Summary

We have identified for the first time a large sample of spectroscopically confirmed young brown dwarfs within the inner regions of the ONC, including five newly classified M9 objects. From this data we have made an HR diagram and possibly discovered a previously unknown population of  $\sim 10$  Myr old low mass stars within the inner regions of the cluster. We have examined this population in detail and determined that it is not an artifact arising from systematics in the spectral reduction/classification processes. We have ruled out that this population consists primarily of “contaminants” from the surrounding OB1 association. If this population is real, we propose that it was not detected in previous works because of its intrinsic faintness, coupled with extinction effects. Another possible scenario is that these objects constitute a population of scattered light sources. If this hypothesis is correct, these

objects provide indirect observational support for recent theoretical arguments indicating higher disk occultation fractions for young substellar objects in comparison to higher mass CTTS (Walker et al. 2004).

From the HR diagram we have used DM97 tracks and isochrones to infer a mass for each object and constructed the first spectroscopic substellar ( $0.6 > M > 0.02 M_{\odot}$ ) IMF for the ONC. Our mass function peaks at  $\sim 0.2 M_{\odot}$  consistent with previous IMF determinations (M02; HC00; Luhman et al. 2000), however it drops off more sharply past  $\sim 0.1 M_{\odot}$  before roughly leveling off through the substellar regime. We compare our mass function to those derived for Taurus and IC 348, also using spectroscopic data, and find remarkable agreement between mass distributions found in IC 348 and the ONC.

## 8. Acknowledgments

The authors would like to thank Davy Kirkpatrick for useful comments which improved the final paper, and Kevin Luhman and Lee Hartmann for their insights and suggestions which helped in our analysis. We thank Alice Shapley and Dawn Erb for sharing their method of subtracting sky lines from NIRSPEC images, as well as NIRSPEC support astronomers Greg Wirth, Grant Hill and Paola Amico for their guidance during observing. We are also appreciative of Michael Meyer for his participation in the CRSP data acquisition and for assistance at the KPNO 4m telescope from Dick Joyce. Finally, we thank LRIS observers N. Reid and B. Schaefer for obtaining several spectra for us. C. L. S. acknowledges support from a National Science Foundation Graduate Research Fellowship.

## REFERENCES

Bally, J., O'Dell, C.R., & McCaughrean M.J. 2000, AJ, 119, 2919

Baraffe, I., Chabrier, G., Allard, F., & Hauschildt, P.H., 1998, A&A, 337, 403

Bessell, M.S. 1991, ApJ, 101, 662

Bessell, M.S., & Brett, J.M. 1988, PASP, 100, 1134

Briceño, C., Luhman, K.L., Hartmann, L., Stauffer, J.R., & Kirkpatrick, J.D. 2002, ApJ, 580, 317

Brown, A.G.A., de Geus, E.J., & de Zeeuw, P.T 1994, A&A, 289, 101

Cardelli, J.A., Clayton, G.C., & Mathis, J.S. 1989, ApJ, 345, 245

Carpenter, J.M., Hillenbrand, L.A., & Strutskie, M.F. 2001, AJ, 121, 3160

Chabrier, G., Baraffe, I., Allard, F. & Hauschildt, P. 2000, ApJ, 542, 464

Cohen, J.G., Frogel, J.A., Persson, S.E., & Elias, J.H. 1981, ApJ, 249, 481

Cohen, M., & Kuhi, L. V. 1979, ApJS, 41, 743

D'Antona, F., & Mazzitelli, I. 1997, Mem. Soc. Astron. Italiana, 68, 807 (DM97)

Dahn, C.C., et al. 2002, 124, 1170

Delgado-Donate, E. J., Clarke, C. J., & Bate, M. R. 2004, MNRAS, 347, 759

Gorlova, N.I., Meyer, M.R., Rieke, G.H., & Liebert, J. 2003, ApJ, 593, 1074

Hillenbrand, L.A., & White, R.J. 2004, ApJ, in press

Hillenbrand, L.A., & Carpenter, J.M. 2000, ApJ, 540, 236 (HC00)

Hillenbrand, L.A., Strom, S. E., Calvet, N., Merrill, K.M., Gatley, I., Makidon, R.M., Meyer, M.R., & Skrutskie, M.F. 1998, AJ, 116, 1816

Hillenbrand, L. A. 1997, AJ, 113, 1733 (H97)

Jones, B.F., & Walker, M.F. 1988, AJ, 95, 1755

Joy, A.H. 1949, ApJ, 110, 424

Kleinmann, S.G., & Hall, D.N.B. 1986, ApJS, 62, 501

Kroupa, P., Bouvier, J., Duchne, G., & Moraux, E. 2003, MNRAS, 346, 354

Lada, C.J., Muench, A.A., Haisch, K.J., Lada, E.A., Alves, J., Tollestrup, E.V., & Willner, S.P. 2000, AJ, 120, 3162

Leggett, S.K., et al. 2002, ApJ, 564, 452

Leggett, S.K., Allard, F., Berriman, G., Dahn, C.C., & Hauschildt, P.H. 1996, *ApJS*, 104, 117

Luhman, K.L. 2000, *ApJ*, 544, 1044

Luhman, K.L., Briceño, C., Stauffer, J.R., Hartmann, L., Barrado y Navascus, D., & Nelson, C. 2003a, *ApJ*, 590, 348

Luhman, K.L., Reike, G.H., Young, E.T., Cotera, A.S., Chen, H., Rieke, M.J., Schneider, G., & Thompson, R.I. 2000, *ApJ*, 540, 1016

Luhman, K.L., Stauffer, J.R., Muench, A.A., Rieke, G.H., Lada, E.A., Bouvier, J., & Lada, C.J. 2003b, *ApJ*, 593, 1093

McGovern, M.R., Kirkpatrick, J.D., McLean, I.S., Burgasser, A.J., Prato, L., & Lowrance J. 2004, *ApJ*, 600, 1020

McClean, I.S., McGovern M.R., Burgasser, A.J., Kirkpatrick, J.D., Prato, L., & Kim, S.S. 2003, *ApJ*, 596, 561

McLean, I.S., et al. 2000, *ApJ* 533, 45

Meyer, M.R., Calvet, N., & Hillenbrand, L.A. 1997, *AJ*, 114, 288

Muench, A.A., Lada, E.A., Lada, C.J., & Alves, J. 2002, 573, 366 (M02)

Muench, A.A., Alves, J., Lada, C.J., & Lada, E. A. 2001, *ApJ*, 558, L51

Prosser, C.F., Stauffer, J.R., Hartmann, L. W., Soderblom, D.R., Jones, B.F., Werner, M.W., & McCaughrean, M.J. 1994, *ApJ*, 421, 517

Reid, I.N., Burgasser, A.J., Cruz, K.L., Kirkpatrick, J.D., & Gizis, J.E. 2001, *AJ*, 121, 1710

Reid, I.N., et al. 1999, *ApJ*, 521, 613

Salpeter, E.E. 1995, *ApJ*, 121, 161

Tokunaga, A.T., & Kobayashi, N. 1999, *AJ*, 117, 1010

Wainscoat, R.J., Cohen M., Volk, K., Walker, H.J., & Schwartz, D.E. 1992, *ApJS*, 83, 111

Walker, C., Wood, K., Lada, C.J., Robitaille, T., Bjorkman, J.E., & Whitney, B. 2004, *MNRAS*, in press

Wilking, B.A., Greene, T.P., & Meyer, M.R. 1999, *AJ*, 117, 469

Wilking, B.A., Meyer, M.R., Greene, T.P., Mikhail, A., & Carlson G. 2004, *AJ*, 127, 1131

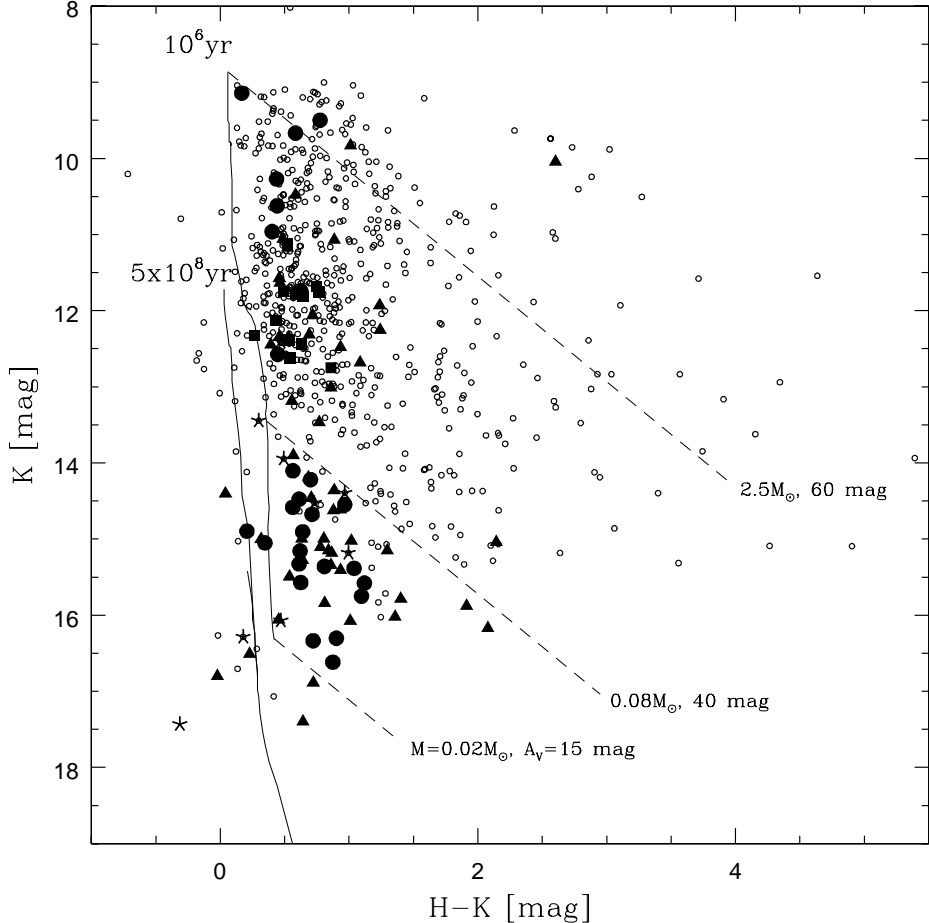


Fig. 1.—  $K$ ,  $(H - K)$  color-magnitude diagram for the ONC. Isochrones are from DM97 and have been transformed into the  $K$ ,  $(H - K)$  plane assuming the age ( $\lesssim 1$  Myr) and distance (480 pc) of the ONC. Dashed lines are reddening vectors emanating at the indicated masses from the 1 Myr isochrone. Open circles represent HC00 photometry of the inner  $5'.1 \times 5'.1$  of the nebula. Sources for which we have  $J$ -band or  $K$ -band spectra taken with NIRSPEC are marked as solid circles and triangles, respectively. Stars were selected for spectroscopy based on their location on the CMD below  $0.08 M_{\odot}$ . Often it was possible to place multiple stars on the slit due to the high stellar density of the cluster, allowing us to observe several brighter (more massive) stars. Starred points indicate sources for which we have new red optical LRIS spectral classifications. Solid squares represent sources (mostly in the outer nebula) for which we have  $J$  &  $K$ -band spectra taken with CRSP.

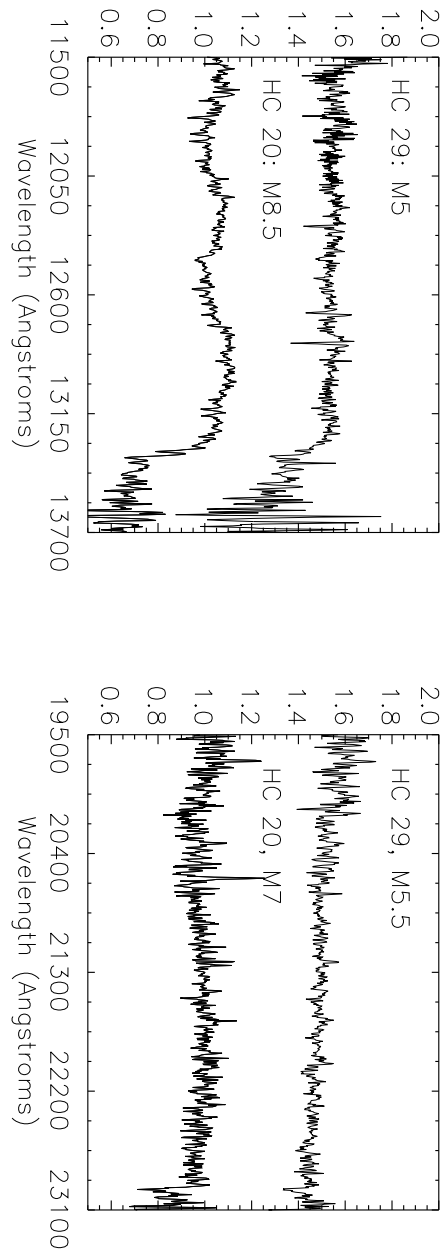


Fig. 2.— NIRSPEC spectra representative of the typical S/N for our program objects. Both targets have relatively low extinction ( $A_V < 5$ ). Derived spectral types are indicated and demonstrate the degree of agreement between  $J$  and  $K$ -band spectral types when both data are available.

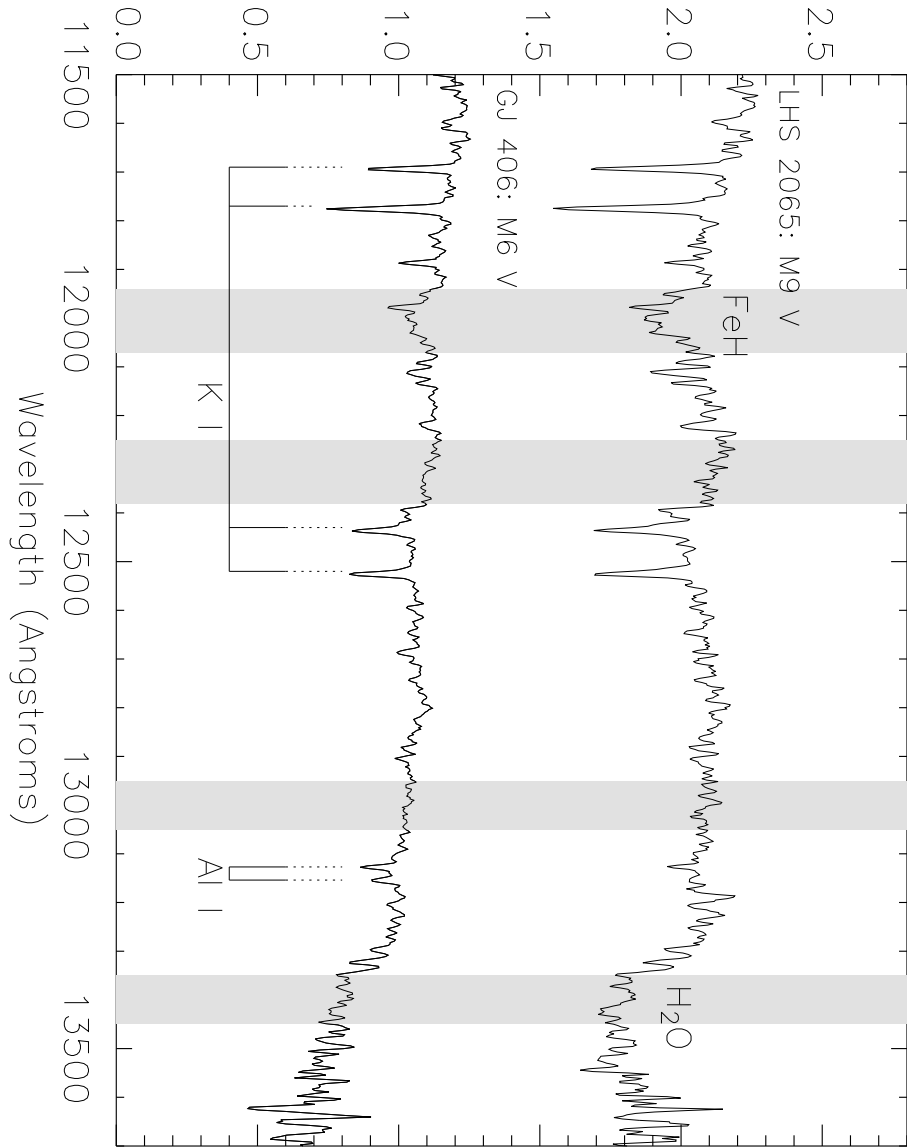


Fig. 3.— *J*-band NIRSPEC spectra of standard stars at two temperatures. The more prominent atomic (pairs of KI doublets and an Al I doublet) and temperature-sensitive molecular features (FeH and H<sub>2</sub>O) are labeled. Flux bands centered on molecular and continuum features used in classification are shown as shaded regions.

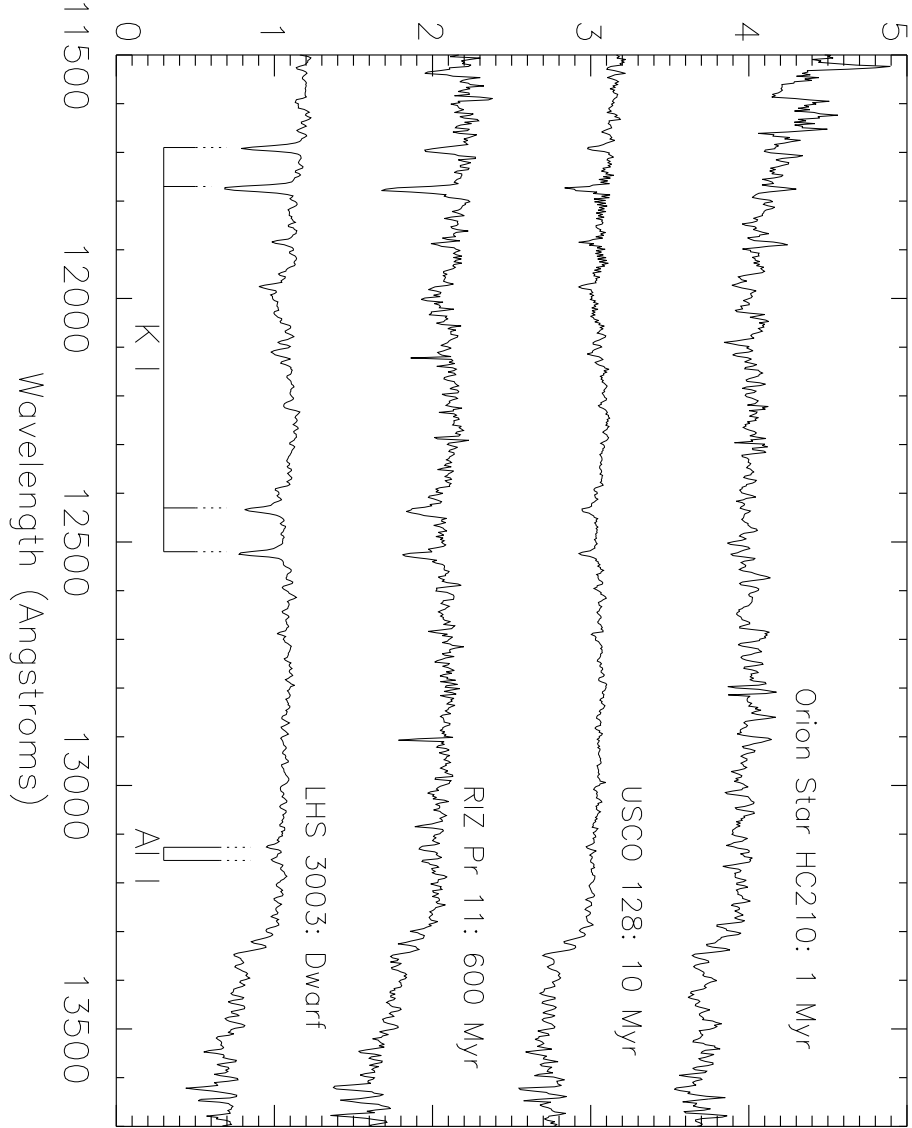


Fig. 4.—  $J$ -band NIRSPEC data of four spectral class M7-M8 stars: an optically-classified main sequence dwarf star (LHS 3003), a newly classified lower surface gravity star in Praesepe (RIZ Pr 11), an optically-classified star in Upper Sco (USCO 128), and a newly classified Orion Star (HC210). Strongly surface gravity sensitive atomic features KI & AlI are labeled.

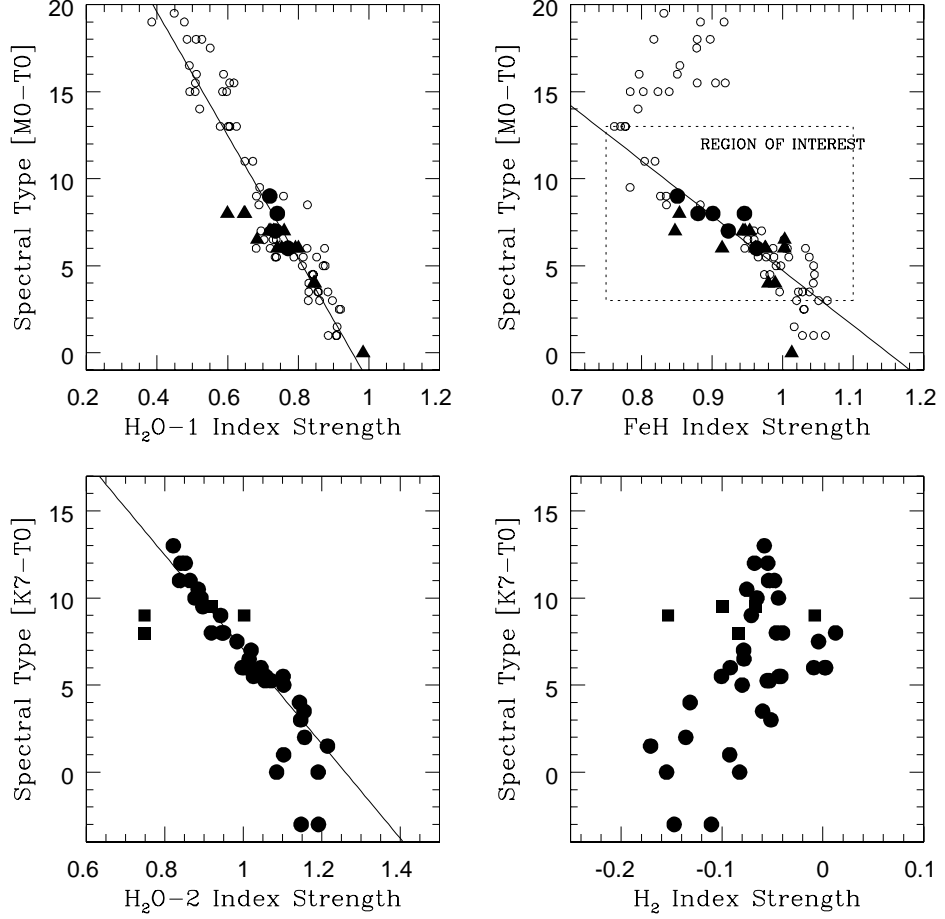


Fig. 5.— Spectral type as a function of classification indices. Solid circles and triangles represent main-sequence standard stars, and lower surface gravity pre-main-sequence taken with NIRSPEC, respectively. Solid squares correspond to giant stars. Open circles are nearby field star and brown dwarf data from the Leggett group. Solid lines are empirical fits listed in Table 2. The FeH index works well only for a limited range in spectral type (M3-L3) where the absorption feature peaks in strength. The  $H_2O$ -2 index works well for objects later than M2. We do not derive an empirical fit to the  $H_2$  index because its dynamic range is small and the scatter significant.

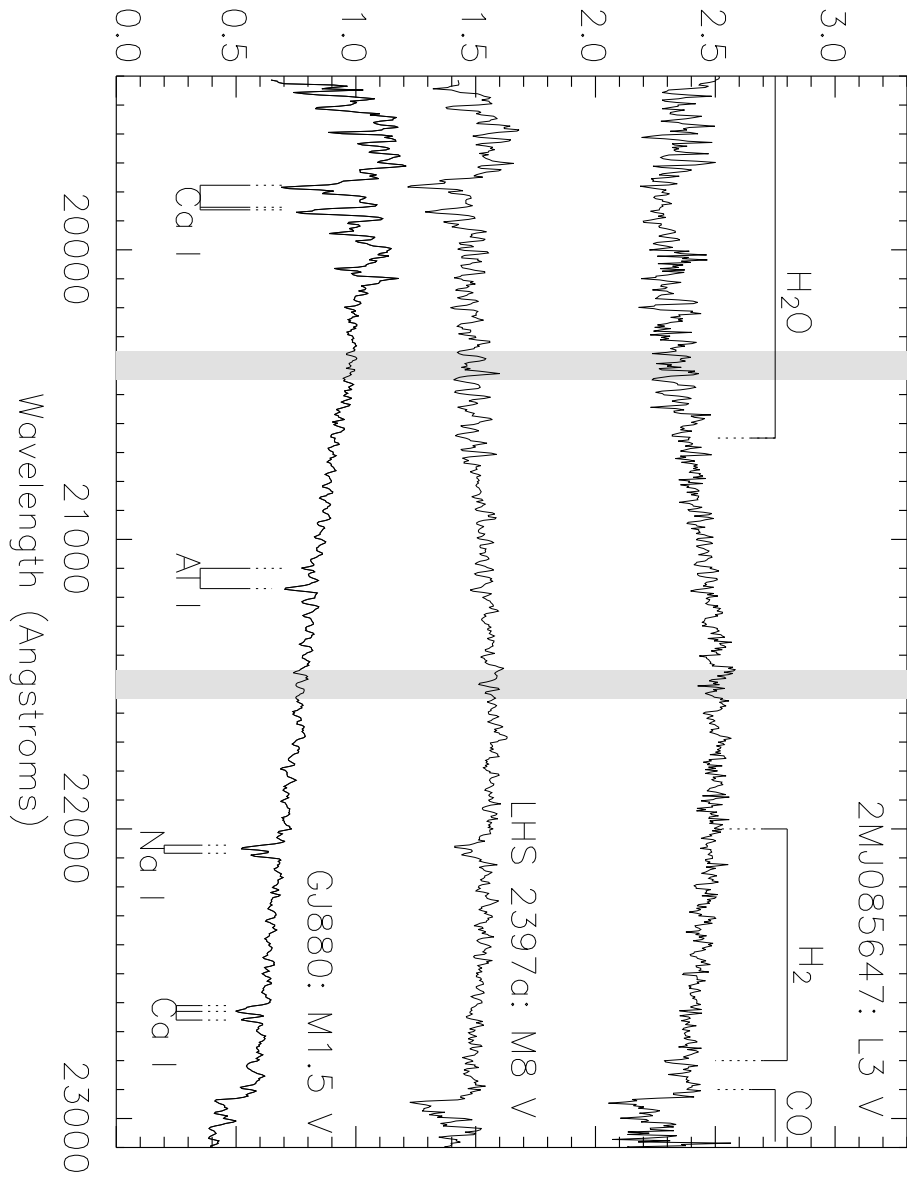


Fig. 6.—  $K$ -band spectra of standard stars taken over a wide range in temperature. Atomic lines (CaI, AlI and NaI) and molecular features ( $\text{H}_2\text{O}$ ,  $\text{H}_2$  and CO) are labeled. Flux bands centered on  $\text{H}_2\text{O}$  and continuum features used in classification are shown as shaded regions.

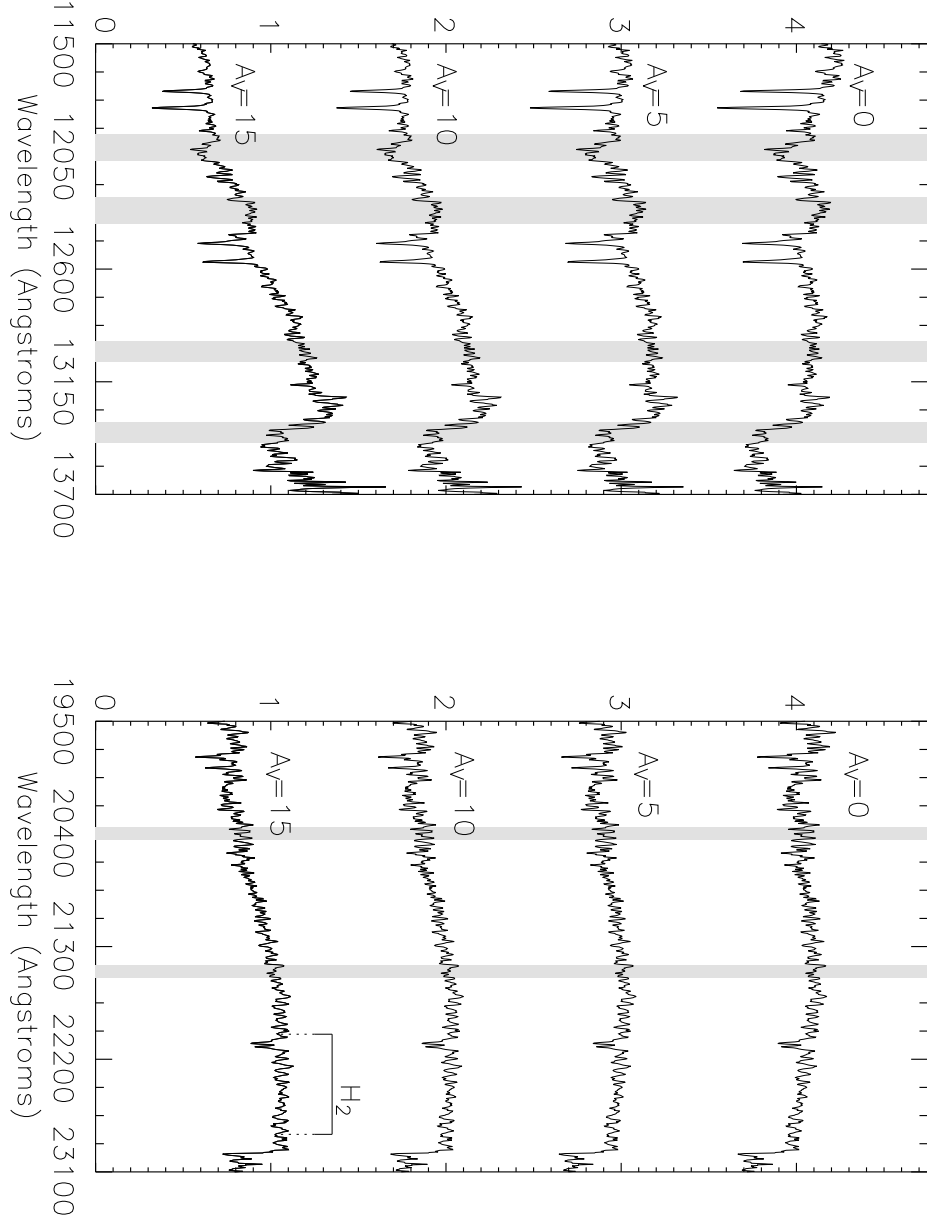


Fig. 7.— M9 main-sequence standard star (LHS 2065) which was observed during both NIRSPEC observing runs ( $K$  &  $J$ -Band). In each panel, the top spectrum is the original data. Subsequent spectra have been artificially reddened by 5, 10 and 15 magnitudes of visual extinction. The flux bands corresponding to classification indices described in the text are shown as shaded regions and the  $K$ -band  $H_2$  absorption region is marked. We expect a systematic shift in all of the indices with increased reddening.

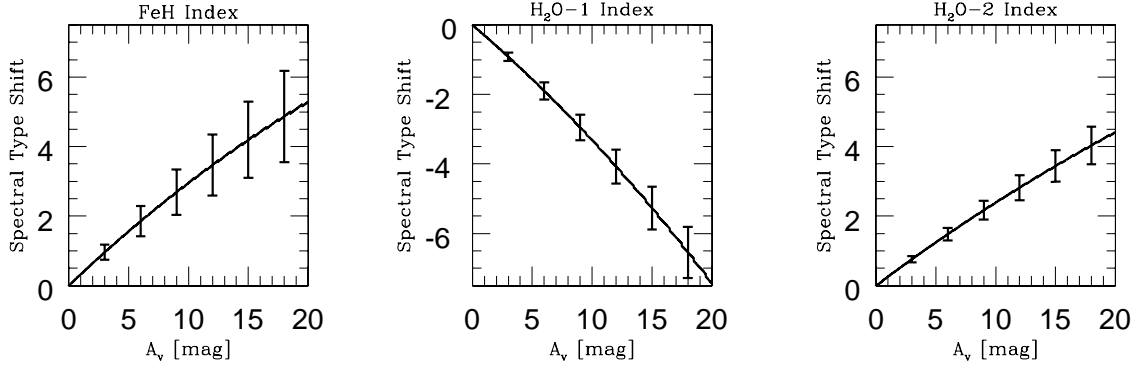


Fig. 8.— Spectral type shift produced from index measurements as a function of  $A_V$ . Extinction causes us to systematically classify a star later than it is using the FeH and H<sub>2</sub>O-2 indices, and earlier than it is using the H<sub>2</sub>O-1 index. Error bars correspond to errors in the fit, which increase with increasing  $A_V$ . We find an average value of  $A_V \sim 6$  for our objects, which would result in a spectral type shift of  $\sim 2$  sub-types for all indices if we did not attempt to take extinction into account during the classification process.

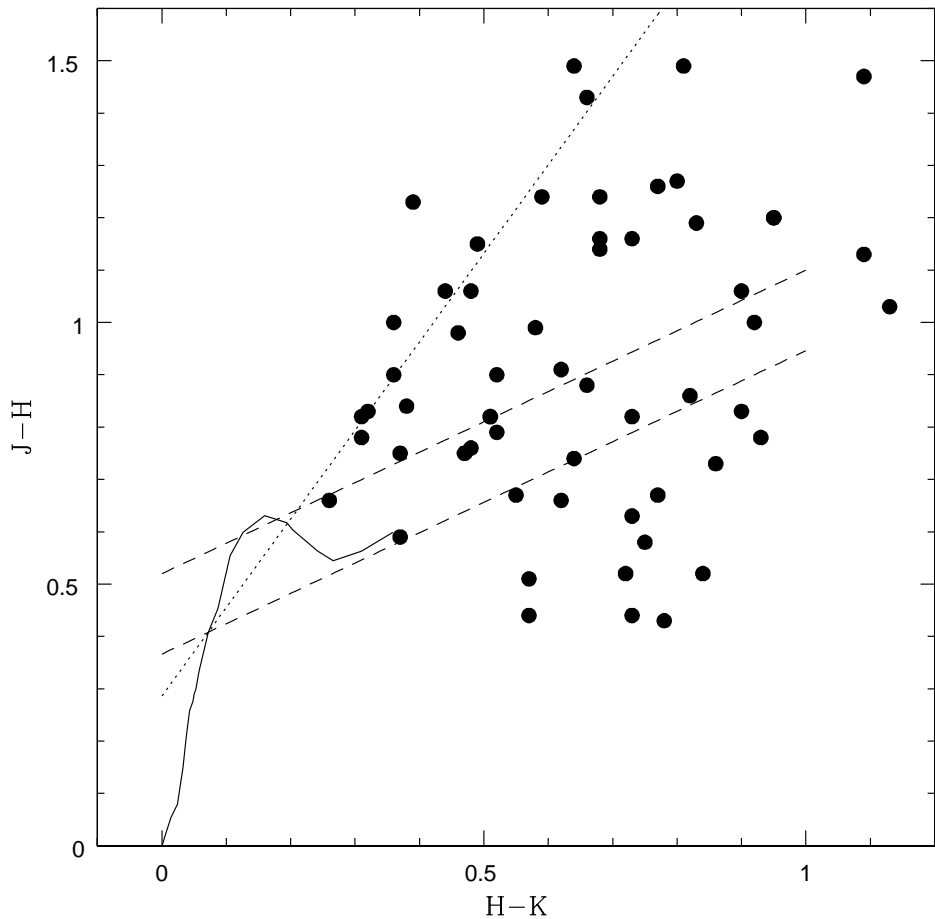


Fig. 9.— Color-color diagram of ONC stars for which we have new near-IR spectral types later than K7. Data are taken from M02. The solid line represents the intrinsic colors of main-sequence dwarf stars as given by Bessell & Brett (1988), transformed to the CIT photometric system. The slope of the interstellar reddening vector (dotted line) is that of Cohen et al. (1981). Dashed lines indicate the upper and lower boundaries of the CTTS locus (Meyer, Calvet & Hillenbrand, 1997) shifted to apply to K7-L3 dwarfs. Note that we have not accounted for the intrinsic width of the locus as it is defined, or any possible change in slope of the locus with later spectral types. If attributed to reddening, the width of the region corresponds to  $\Delta A_V \sim 2$ , or less than one spectral subtype (see Figure 8).

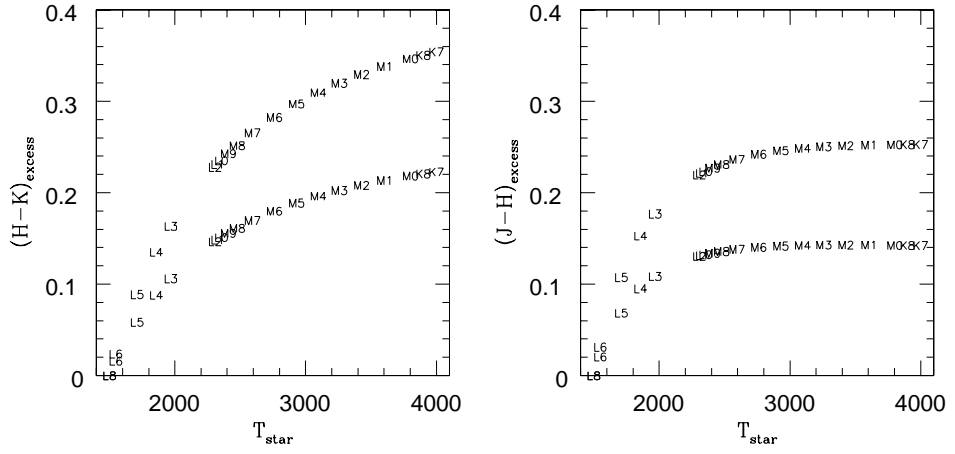


Fig. 10.— Expected color excess for low mass stars veiled by a  $T=1500$  K blackbody. Data points are labeled by spectral type and the two rows correspond to  $r_K = 0.5$  (bottom) and 1 (top). For  $r_K < 0.5$ , we expect color excesses  $\Delta(H - K)$  and  $\Delta(J - H) \lesssim 0.2$  mag. The effect of veiling on classification is  $\approx 1.5\text{--}2$  spectral subclasses earlier for the H<sub>2</sub>O-2 and FeH indices and later for the H<sub>2</sub>O-1 index.

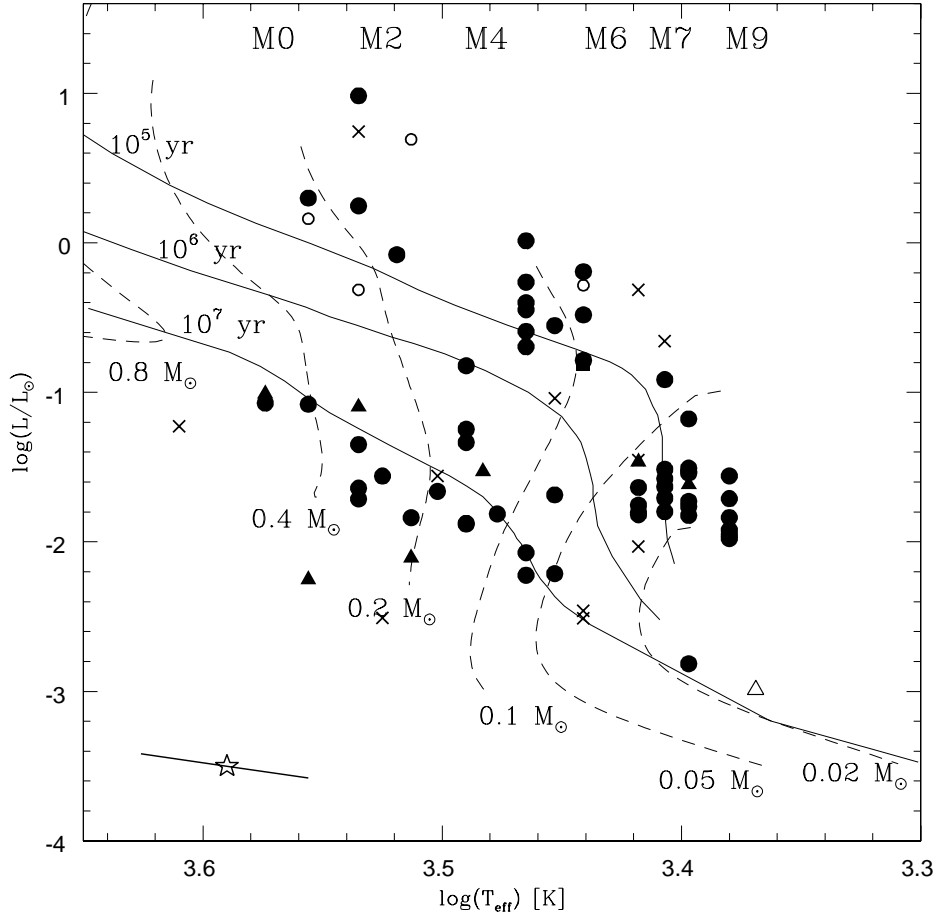


Fig. 11.— HR diagram of objects within the inner  $5.1 \times 5.1$  of the ONC (survey area of HC00) for which we have new spectral types. Filled symbols correspond to stars classified using NIRSPEC and CRSP infrared observations which have good spectral types. Objects which were classified as “high” gravity (i.e., had strong absorption lines, similar in strength to dwarf stars of the same temperatures) are marked as open symbols and objects with less certain spectral types (those designated with a “:” in Table 1a) are marked as X’s. Triangles represent objects which have new optical spectral types taken with LRIS. A typical error bar for an  $M6 \pm 1.5$  star is shown in the lower left corner. The pre-main-sequence model tracks and isochrones of DM97 are also shown.

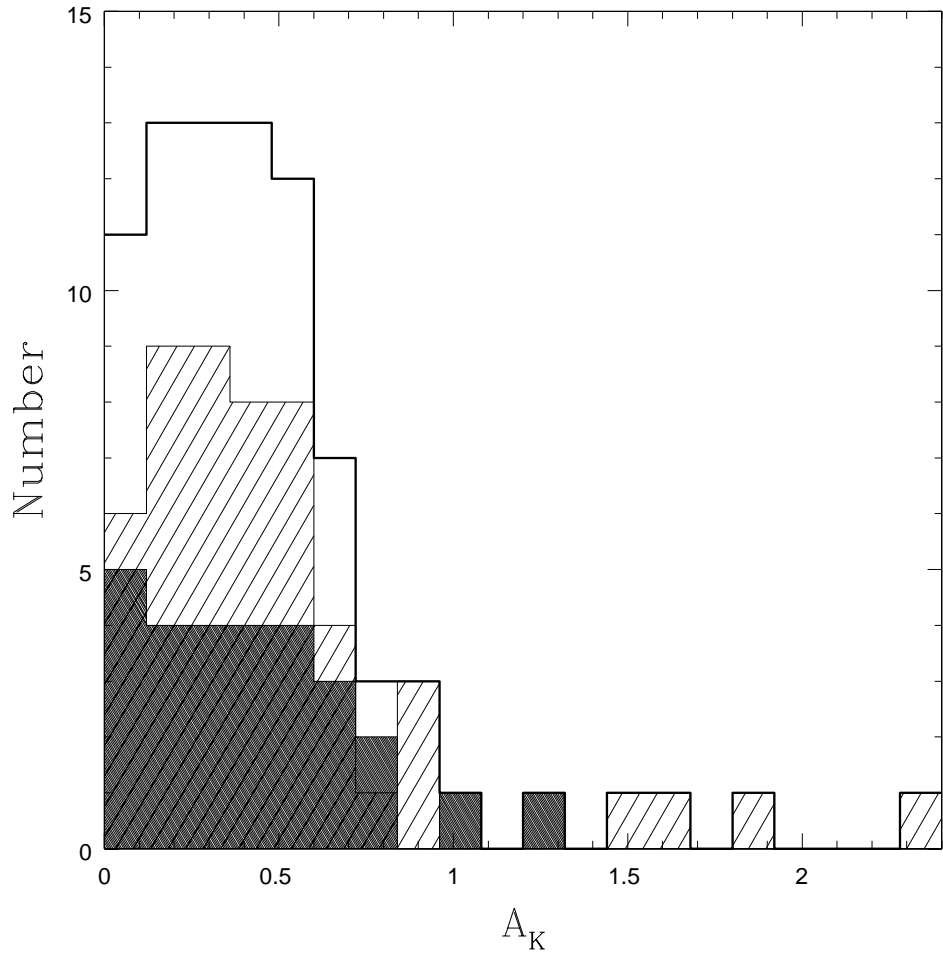


Fig. 12.— Histogram of extinction for sources included in Figure 11. The open histogram indicates all objects; the hatched and shaded histograms include the two populations with apparent ages (as interpreted from the HR diagram) of  $\sim 1$  and  $\sim 10$  Myr old, respectively. We find similar extinction distributions for all three populations.

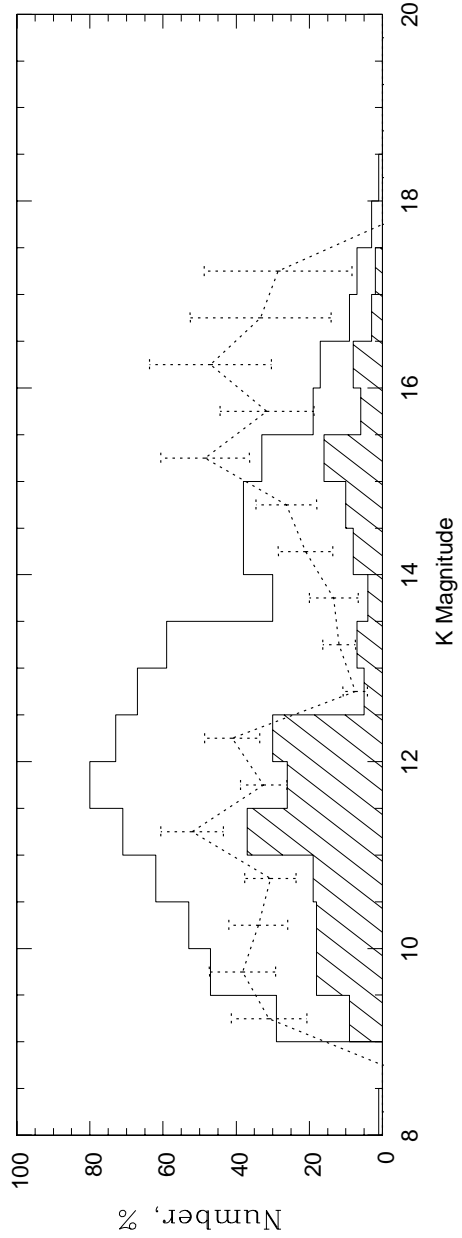


Fig. 13.— Histogram of HR diagram completeness as a function of magnitude. Open and hatched histograms indicate the distribution of all HC00 photometry and the subset for which we have spectral types, respectively. The dotted line in each panel indicates fractional completeness of the spectroscopic sample with  $\sqrt{N}$  errorbars. Although the spectroscopic sample is  $\approx 40\%$  complete at bright and faint magnitudes, correction factors to the mass function are needed at intermediate magnitudes.

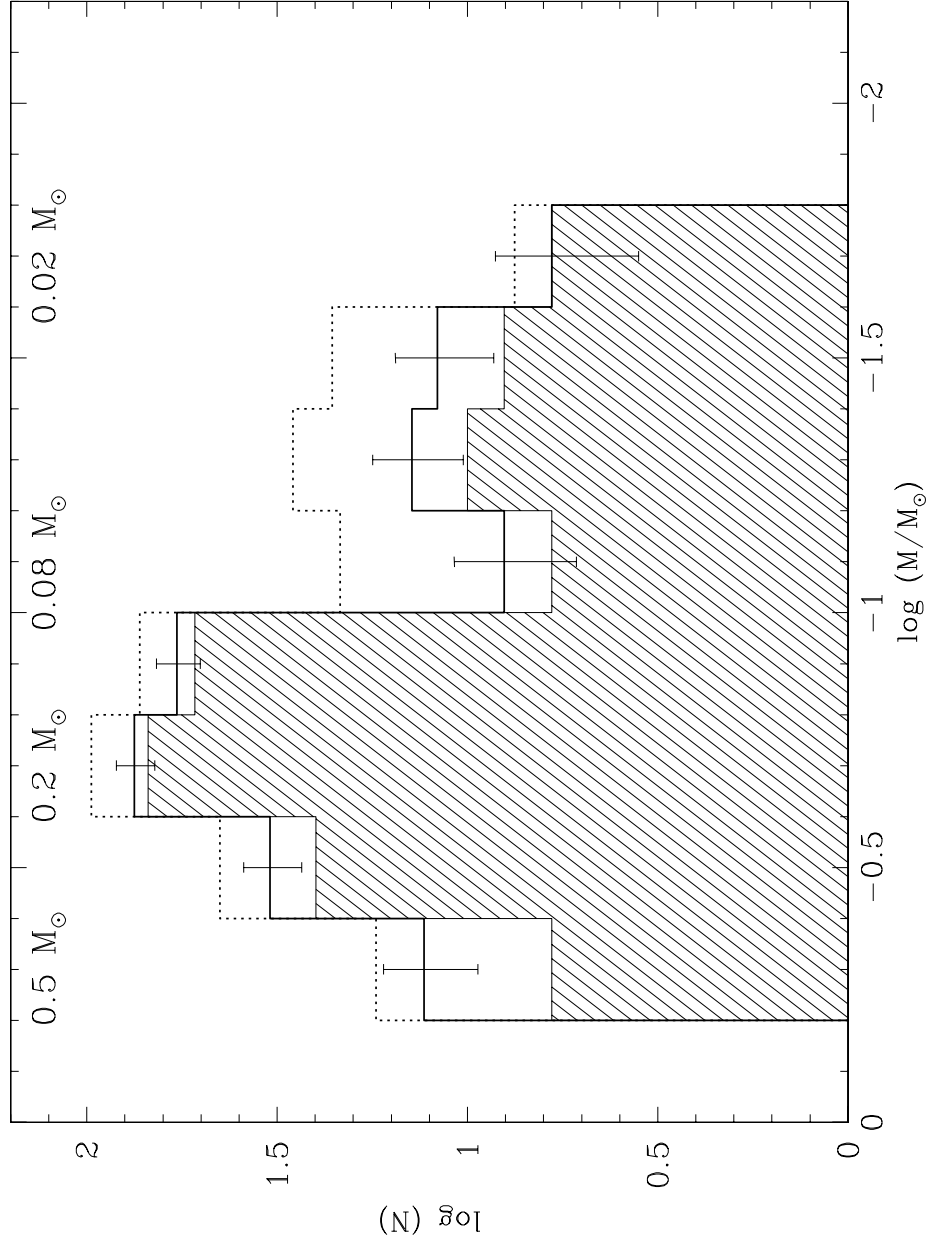


Fig. 14.— Mass function for all stars within the inner  $5.^{\circ}1 \times 5.^{\circ}1$  of the ONC that have spectral types from the present work or the literature later than M0. Thick-lined open histogram shown with  $\sqrt{N}$  errorbars indicates all stars; the dotted open histogram represents the same sample corrected for incomplete magnitude bins (Figure 13). The hatched histogram indicates only stars younger than  $\sim 5$  Myr according to the HR diagram (Figure 11).

Table 1a. Band Indices & Spectral Types for the Inner 5.'1×5.'1 of the ONC

ID <sup>a</sup>	K <sup>a</sup>	J-Band		K-Band		Spectral Type	Gravity <sup>d</sup>	Comments <sup>e</sup>
		H <sub>2</sub> O-1	FeH	H <sub>2</sub> O-2	H <sub>2</sub>			
4	14.91	0.799	1.017	...	...	M4.5	M5.5	low
15	15.36	0.921	0.974	...	...	M0-M1	M3.5	...
20	14.19	0.639	0.959	0.985	-0.018	...	M8	low
22	13.19	...	...	0.997	-0.014	...	M8	int
25	13.90	...	...	1.189	-0.167	M: <sup>f</sup>	M1	low/int
27	16.30	0.801	0.962	...	...	...	M5	low
29	11.74	0.827	0.987	1.032	-0.040	...	M5	low
30	15.05	0.877	1.020	...	...	M0-3	M2	low
35	11.11	...	...	...	...	M3.5 <sup>f</sup>	M7; <sup>g</sup>	...
48	15.57	0.839	0.974	...	...	...	M4	low
51	11.63	...	...	1.017	-0.013	...	M5	int
55	14.10	0.736	0.934	...	...	...	M8	low
59	16.29	...	...	...	...	K8-M3	...	...
62	15.34	...	...	0.879	0.039	...	M9	low
64	14.52	...	...	...	...	M7-9	...	low
70	15.75	0.624	0.870	...	...	...	M9	low
90	13.01	...	...	0.953	0.030	...	M7.5	int
91	14.90	0.892	1.093	...	...	...	<K7 <sup>h</sup>	...
93	9.50	0.859	0.982	...	...	M3e <sup>f</sup>	M3	high
111	15.38	0.704	0.943	...	...	...	M9	low
114	13.94	...	...	...	...	M7	...	low
123	14.61	...	...	0.977	0.031	M0-5	M7.5	low
127	14.55	0.960	1.021	...	...	...	M0	int
143	15.00	...	...	1.152	-0.377	<M2:	M2.5	low
162	12.48	...	...	0.979	-0.035	...	M5.5	low
167	15.02	...	...	0.942	-0.007	M6-8	M7.5	low
200	15.49	...	...	1.145	-0.159	...	M3	...
210	14.68	0.732	0.996	...	...	>M6:	M7	low
212	14.22	0.683	0.904	...	...	...	M9	low
221	14.46	...	...	0.949	-0.038	...	M7.5	low
227	10.96	0.892	1.105	...	...	M1	<K7 <sup>h</sup>	...
237	13.44	...	...	...	...	M2	...	CalIe
264	12.41	...	...	...	...	M6 <sup>f</sup>	M6 <sup>g</sup>	...
288	10.62	0.921	0.982	...	...	K8 <sup>f</sup>	M1	high
290	13.47	...	...	0.989	-0.013	...	M5.5:	...
293	9.14	0.700	1.283	...	...	B8	<K7 <sup>h</sup>	low
316	15.18	...	...	...	...	M3.5-5	...	CalIe
346	10.48	...	...	1.120	-0.106	...	M2	low/int
355	12.35	...	...	1.054	-0.067	...	M5	int
365	15.40	...	...	0.918	0.004	...	M7:	...
366	12.68	...	...	0.926	0.024	...	M7.5	low
368	11.07	...	...	1.014	-0.025	...	M5	int
372	14.48	0.677	0.958	...	...	...	M9	low
381	11.06	...	...	1.129	-0.112	M2 <sup>f</sup>	M1.5-4	int

Table 1a—Continued

ID <sup>a</sup>	K <sup>a</sup>	J-Band		K-Band		Spectral Type	Gravity <sup>d</sup>	Comments <sup>e</sup>
		H <sub>2</sub> O-1	FeH	H <sub>2</sub> O-2	H <sub>2</sub>			
383	14.36	0.922	0.869	1.066	-0.121	...	M4	low
395	9.83	...	...	1.016	-0.040	...	M2:	...
396	11.93	...	...	1.006	-0.026	M: <sup>f</sup>	M4-8	int
400	15.16	0.694	0.913	...	...	M7-8	M9	low
403	15.15	...	...	0.930	0.005	...	M7	low
409	14.39	...	...	...	...	M0	...	possible NIR emission lines
429	15.11	...	...	0.938	0.031	M7-9	M7.5	low
433	15.58	0.695	0.994	...	...	...	M8	low
434	10.04	...	...	0.949	0.022	...	M2	...
454	12.06	...	...	1.055	-0.068	...	M2	high
455	15.84	...	...	0.995	-0.066	...	M2-6	...
459	12.34	...	...	1.072	-0.051	...	M6	int
467	11.17	...	...	1.056	-0.050	M2-4 <sup>f</sup>	M6	high
469	14.74	...	...	...	...	M	...	...
509	15.33	0.900	0.988	0.986	-0.126	M2-5	M2-7	...
515	15.88	...	...	0.804	0.088	...	M7:	low
529	16.17	...	...	0.775	0.151	...	M8	low
543	10.27	0.931	0.977	...	...	M2.5 <sup>f</sup>	M1	int/high
553	12.31	...	...	1.043	-0.035	...	M5	low/int
555	11.58	...	...	1.090	-0.049	...	M6	...
559	14.40	...	...	0.958	-0.017	...	M8	low
565	15.00	...	...	0.930	0.048	...	M8	low
568	15.00	...	...	0.808	0.172	...	<K7 <sup>h</sup> :	...
594	14.58	0.776	1.039	...	...	...	M7.5	low
600	12.25	...	...	0.979	0.056	...	M5	low
684	14.66	...	...	1.094	-0.081	...	M0-4	...
687	15.28	...	...	1.110	-0.118	...	M0-4	...
708	15.04	...	...	0.905	0.098	...	M4	low
709	16.06	...	...	0.854	0.041	...	M5	low
721	15.18	...	...	0.995	-0.102	...	M3.5:	...
722	17.43	...	...	...	...	L0	...	high
723	16.07	...	...	...	...	M3	...	low
724	16.51	...	...	1.218	-0.044	...	M6:	...
725	16.07	...	...	0.916	0.041	...	M7:	...
728	16.34	0.772	1.074	...	...	...	M5.5	low
729	16.02	...	...	0.861	0.032	...	M7	low
730	15.15	...	...	1.111	-0.114	...	M4	low
731	15.79	...	...	1.061	-0.125	...	K7:	...
732	16.80	...	...	1.029	0.046	...	M2.5:	...
743	16.89	...	...	0.997	-0.055	...	M6:	...
749	17.40	...	...	1.001	0.075	...	M8	...
764	14.62	...	...	0.974	-0.194	K8-M3	M7.5:	...

<sup>a</sup>IDs and *K* magnitudes from Hillenbrand & Carpenter, 2000.<sup>b</sup>Optical spectral types are from LRIS data presented here, unless otherwise noted.

<sup>c</sup>Uncertainties in infrared spectral types are  $\pm 1.5$  sub-class unless otherwise noted. A ":" indicates the spectrum had lower S/N and the classification is less certain.

<sup>d</sup>For *J*-band spectra, an object was given a gravity classification of "low" if it had no detectable atomic absorption lines and "high" if it had strong lines, similar to those seen in spectra of dwarf standards of same spectral types. A classification of "int" indicates absorption lines were present but not as strong as those in dwarf stars at the same temperatures. For *K*-band spectra gravity classifications were determined based on the relative atomic line ratios. A " ..." indicates the S/N of the spectra was not sufficient to determine if absorption lines were present.

<sup>e</sup>A comment of "possible NIR emission lines" indicates that residual emission lines were present after background sky subtraction which may originate from the star rather than the nebula. However, due to the very high background of nebular emission, we cannot say with certainty that this is the case. This comment primarily refers to H<sub>2</sub> seen in emission. P cygni profile labels are given as uncertainties for the same reason.

<sup>f</sup>Optical spectral type from Hillenbrand 1997.

<sup>g</sup>Classification from CRSP spectrum.

<sup>h</sup>We did not attempt to classify objects earlier than K7.

Table 1b. Spectral Types for the Outer<sup>a</sup> ONC

ID <sup>b</sup>	<i>K</i> <sup>b</sup>	Spectral Type	
		Optical <sup>c</sup>	IR <sup>d</sup>
1	12.49	M5.5 <sup>e</sup>	M6
205	11.68	M6 <sup>e</sup>	M7
615	12.32	M6 <sup>e</sup>	M7
649	12.13	M6 <sup>e</sup>	M8
689	12.75	M5.5 <sup>e</sup>	M6
711	...	M6 <sup>e</sup>	M7:
806	12.32	M5.5	M6.5
859	11.75	M5 <sup>e</sup>	M8
974	11.38	M5.5	M6-8
1036	12.38	M6 <sup>e</sup>	M6
3017	12.62	M4.5 <sup>e</sup>	M2-5
3039	11.76	M5.5	M7
3046	11.79	M5.5	M5
5100	11.81	M5.5e <sup>e</sup>	M6

<sup>a</sup>Outer in this context refers to beyond the 5.'1×5.'1 NIRC field centered on  $\theta^1\text{C}$ .

<sup>b</sup>IDs and *K* magnitudes from Hillenbrand et al., 1998. See references therein.

<sup>c</sup>Optical spectral types are from LRIS data, unless otherwise noted.

<sup>d</sup>Infrared spectral type uncertainties are  $\pm 2$  sub-class unless otherwise noted. A ":" indicates the spectrum had lower S/N and the classification is less certain.

<sup>e</sup>Optical spectral types come from Hillenbrand 1997.

Table 2. Empirical Relations

Fit	Error	Range	Comment
Sp type = $(33.71 \pm 0.79) - (35.35 \pm 1.06) * (H_2O-1)$	$\sigma = \pm 1.2$	M0-T0	In the spectral type relations for band index fits M0 is represented by 0, M5 by 5, and L0 by 10. All Sp type equations assume dereddened band index measurements.
Sp type = $(36.31 \pm 1.46) - (31.59 \pm 1.59) * (FeH)$	$\sigma = \pm 0.66$	M3-L3	
Sp type = $(34.13 \pm 1.19) - (27.10 \pm 1.20) * (H_2O-2)$	$\sigma = \pm 0.53$	M2-L3	
$T_{eff} = -224536 + 111513 * (\text{Sp type}) - 17907.9 * (\text{Sp type})^2 + 943.944 * (\text{Sp type})^3$	$\sigma = \pm 33.9$	K7-L0	In the spectral type relations for HR diagram transforms
$(H - K)_o = 51.4776 - 23.9402 * (\text{Sp type}) + 3.67070 * (\text{Sp type})^2 - 0.184388 * (\text{Sp type})^3$	$\sigma = \pm 0.033$	K7-L0	M0 is represented by 6.0, M5 by 6.5, and L0 by 7.0.
$BC_K = 57.1637 - 27.7257 * (\text{Sp type}) + 4.54411 * (\text{Sp type})^2 - 0.240687 * (\text{Sp type})^3$	$\sigma = \pm 0.037$	K7-L0	

Table 3. Derived Quantities for Stars in the HR Diagram

ID	$A_V$ [mag]	$\log T_{eff}$ [K]	$\log L/L_\odot$	$M/M_\odot$
4	4.67	3.453	-1.686	0.08
15	8.47	3.502	-1.662	0.19
20	3.77	3.397	-1.507	0.04
22	1.78	3.397	-1.178	0.05
25	6.00	3.556	-1.080	0.42
27	9.00	3.465	-2.072	0.08
29	4.77	3.465	-0.400	0.11
30	2.18	3.535	-1.713	0.31
35	1.94	3.418	-0.315	0.10
48	5.37	3.490	-1.876	0.15
51	2.26	3.465	-0.447	0.11
55	1.90	3.397	-1.540	0.03
59	0.02	3.556	-2.251	0.34
62	5.85	3.380	-1.920	0.02
64	4.46	3.397	-1.617	0.03
70	9.48	3.380	-1.953	0.02
90	6.77	3.407	-0.915	0.07
93	8.24	3.513	0.692	0.18
111	8.61	3.380	-1.837	0.03
114	1.44	3.418	-1.464	0.05
123	7.89	3.407	-1.515	0.04
127	12.51	3.574	-1.072	0.58
143	6.31	3.525	-1.560	0.27
162	9.17	3.453	-0.553	0.11
167	9.19	3.407	-1.631	0.03
200	4.58	3.513	-1.838	0.22
210	4.81	3.418	-1.636	0.04
212	3.41	3.380	-1.559	0.03
221	4.43	3.407	-1.577	0.04
237	1.44	3.535	-1.097	0.29
264	1.67	3.441	-0.810	0.10
288	4.08	3.556	0.161	0.23
290	6.64	3.453	-1.039	0.11
316	10.89	3.483	-1.529	0.15
346	5.81	3.535	0.247	0.18
355	3.32	3.465	-0.695	0.12
365	8.23	3.418	-1.804	0.04
366	10.25	3.407	-0.657	0.08
368	8.77	3.465	0.014	0.10
372	2.04	3.380	-1.711	0.03
381	3.93	3.519	-0.079	0.17
383	9.35	3.490	-1.247	0.16
395	12.41	3.535	0.744	0.20
396	13.53	3.441	-0.193	0.10
400	2.16	3.380	-1.978	0.02

Table 3—Continued

ID	$A_V$ [mag]	$\log T_{eff}$ [K]	$\log L/L_\odot$	$M/M_\odot$
403	6.78	3.418	-1.754	0.04
409	12.51	3.574	-1.010	0.59
429	5.53	3.407	-1.798	0.03
433	10.44	3.397	-1.823	0.02
434 <sup>a</sup>	21.41	3.535	0.983	0.20
454	7.85	3.535	-0.314	0.23
455	8.21	3.490	-1.881	0.15
459	1.59	3.441	-0.786	0.10
467	2.55	3.441	-0.284	0.10
509	4.86	3.477	-1.813	0.12
515	23.29	3.418	-1.452	0.05
529	25.18	3.397	-1.530	0.03
543	4.00	3.556	0.299	0.21
553	5.77	3.465	-0.592	0.11
555	1.56	3.441	-0.482	0.10
559	0.00	3.397	-1.729	0.03
565	5.60	3.397	-1.764	0.02
594	2.20	3.407	-1.707	0.03
600	14.26	3.465	-0.263	0.11
684	7.93	3.535	-1.349	0.31
687	6.68	3.535	-1.641	0.31
708	28.72	3.490	-0.822	0.15
709	2.11	3.465	-2.223	0.07
721	9.38	3.502	-1.558	0.19
722	0.00	3.369	-2.989	0.02
723	3.55	3.513	-2.106	0.21
724	0.00	3.441	-2.511	0.03
725	9.40	3.418	-2.030	0.03
728	5.91	3.453	-2.213	0.05
729	14.73	3.418	-1.818	0.04
730	15.69	3.490	-1.335	0.17
731	19.53	3.610	-1.228	0.56
732	0.00	3.525	-2.508	0.23
743	5.61	3.441	-2.462	0.03
749	3.10	3.397	-2.815	0.02
764	7.06	3.407	-1.548	0.04

<sup>a</sup>Based on visual inspection of the spectra of HC 434, we find the extinction value derived for this source using the intrinsic colors of a spectral type M2 star to be an over-estimate. Instead we use the extinction derived by dereddening its  $(J - H), (H - K)$  colors back to the CTTS locus (see section 3.4) to determine the derived quantities listed in the table as well to place HC 434 on the HR diagram (Fig. 11).

**Erratum: “The Spectroscopically Determined Substellar Mass Function of the Orion Nebula Cluster” (ApJ, 610, 1045 [2004])**

Catherine L. Slesnick, Lynne A. Hillenbrand, & John M. Carpenter

cls@astro.caltech.edu, lah@astro.caltech.edu, jmc@astro.caltech.edu

In Table 1 object HC-722 was incorrectly classified as an L0 dwarf. The original classification was based on the apparent prominence in the spectrum of the KI doublet ( $\sim 7700$  Å). However, standard stars available to us at the time were of lower resolution (by a factor of  $\sim 2$ ) compared to the program stars. Narrow spectral features such as the KI doublet were thus blurred and appeared weaker. We have since re-analyzed the spectrum of object HC-722 in comparison to higher resolution standards taken with LRIS (the same instrument used to obtain the spectrum of HC-722), and re-classified it as an M6.5 V dwarf object. In table 4 the values for HC-722 should be replaced by:  $\log T_{eff} = 3.429$  K,  $\log L/L_{\odot} = -2.89$ ,  $M = 0.04 M_{\odot}$ .

Note that the object is still considered a dwarf, showing no signs of lower gravity. This, combined with the fact that we derive zero  $A_V$  for HC-722, implies it is likely a foreground field dwarf. If we assume an absolute magnitude  $M_K = 9.85$  mag (Leggett 1992) for an M6.5V star, we derive a distance modulus of 7.58 ( $d \sim 330$  pc). Because HC-722 was previously determined to have higher gravity than members of the ONC it was not included in the derivation or analysis of the cluster IMF. As this “high gravity” assignment is not affected by the re-classification, the change does not alter or impact any of our original conclusions.

**REFERENCES**

Leggett, S.K. 1992, ApJS, 82, 351